Data-Driven Thermal Modelling of Liquid Radioisotope Targets

Miranda Sage Niddrie

Supervised by Morgan Dehnel[1,3,4], Tobias Junginger[1,2], and Cornelia Hoehr[2,3]

[1] *Department of Physics and Astronomy, University of Victoria, Victoria, BC*
[2] *TRIUMF, Vancouver, BC*
[3] *Department of Computer Science, Mathematics, Physics and Statistics, University of British Columbia, Kelowna, BC*
[4] *Accel-Link Ltd., Nelson, BC*

A Thesis Submitted in Partial Fulfillment of the Requirements for the Honours Program in the Department of Physics and Astronomy

Department of Physics and Astronomy
University of Victoria
Victoria, British Columbia, Canada

Abstract

Radioisotopes are extensively used in nuclear medicine for various imaging techniques as well as for therapeutic applications. Some isotopes are produced in nuclear reactors (^{99m}Tc, ^{177}Lu), while other radioisotopes have shown great promise in being manufactured in cyclotrons (^{68}Ga, ^{67}Cu, ^{225}Ac, ^{18}F), resulting in improved safety and lower costs [2]. However, thermodynamic conditions within the accelerator target, in conjunction with the target design, result in a low experimental yield of the desired radioisotope product. Recently, Fibre Bragg Gratings were used as sensors to acquire temperature data during the irradiation of liquid cyclotron targets [1]. Computational modelling within the target was executed to replicate these measurements. The 3D geometry of the target was assembled in SolidWorks based on draft drawings provided by TRIUMF. This geometry was imported into engineering simulation software, ANSYS, to conduct thermal modelling. Beam data was provided by determining the energy deposited by the 13 MeV proton beam in each layer of the target using SRIM/TRIM software. The thermal model was assessed based on its ability to accurately model the experimentally measured temperatures, given the initial conditions of the system. The heat transfer coefficient, h (W/m^2K), for helium cooling was varied in the model to attempt to improve the fit; however, little improvement across the model resulted from these adjustments. By addressing the issue of low cyclotron radioisotope yields through iterative modelling compared to experimental measurements, this work supports the development of more accurate liquid target designs. Once more accurate models of these targets exist, they can be designed to maximize radioisotope production, allowing more patients worldwide to access lifesaving imaging and treatment services.

Table of Contents

List of Tables

List of Figures

ACKNOWLEDGEMENTS

I would like to thank my supervisory committee Dr. Morgan Dehnel, Dr. Tobias Junginger, and Dr. Cornelia Hoehr, for their support and guidance throughout this project. I am grateful for the UVIC Learning and Teaching Innovation Centre providing financial support for this research through a Jamie Cassels Undergraduate Research Award (JCURA). I am honoured to have been recognized at Honours Fest 2026 through the Boehm Family Award for Excellence in Science.

This research was conducted on the traditional unceded territory of the Coast Salish peoples, including the Lekwungen (Songhees and Esquimalt) and WSÁNEĆ peoples. As an uninvited visitor on these lands, I am forever thankful to be able to work, learn, and play in such a beautiful place.

This thesis is dedicated to my partner, Maxwell, and our cat, Cosmo. Both of whom have given me continuous support throughout the five years of this degree.

Chapter 1

Introduction

1.1 Radioisotopes in Medicine

In 2025, the Canadian Cancer Society estimated that there would be 254,800 new cancer cases and 87,400 cancer deaths in Canada over the year [4]. Undiagnosed patients may drive this statistic even higher. When a doctor suspects that a patient may have cancer, a diagnostic imaging test is ordered to help confirm the presence of cancer and determine what stage it is. If the patient does indeed have cancer, they can choose whether or not to pursue with treatment. During treatment, half of the people who develop cancer will receive a form of radiation therapy [5]. Both diagnostic imaging and internal radiation therapy use medical radioisotopes.

Examples of diagnostic imaging modalities include Positron Emission Tomography (PET) and Single-Photon Emission Computed Tomography (SPECT). Both of these techniques are ideal for detecting cancerous tissue as they provide contrast to the more metabolically active regions of the body. Cancer is highly metabolic, rapidly consuming sugars as it metastasizes and grows. PET takes advantage of this, typically using a sugar molecule with a radiotracer, Fluorine-18 (^{18}F), attached to it. As ^{18}F decays, it releases positrons, which are captured by the scanner, creating an image of the patient with key physiological information [6]. SPECT primarily utilizes ^{99m}Tc as the injected radiotracer, with the scanner detecting photons as the radioisotope decays [7].

Brachytherapy is a common form of internal radiation therapy, where sealed radioactive sources are surgically inserted into specific regions of the body to target cancerous tissue [8]. This invasive yet successful procedure is commonly performed for brain, breast, and prostate cancer [8]. The decaying radioisotope damages the DNA of cancer cells, affecting how they divide, and also directly killing them through radiation-induced apoptosis. Radioisotopes commonly used for this procedure include ^{192}Ir, ^{60}Co, and ^{125}I; however, at the start of its invention, Radium was used during treatment [9].

1.2 History of Radioisotope Production

In the early 1900s, Marie Curie discovered that her Nobel-winning isolated element, Radium, had the power to destroy diseased cells faster than healthy cells [9]. This began the era of Nuclear Medicine.

Nuclear Medicine has been rapidly evolving post World War II, with a notable expansion in the fight against cancer using manufactured radioisotopes for treatment and imaging of patients. Originally produced in nuclear reactors, worldwide reactor shutdowns have increased radioisotope production through other means [10]. While it was active, Canada's very own National Research Universal Reactor (NRU) supplied more than 40% of the world's supply of medical isotope ^{99}Mo [10]. As the more stable parent isotope of ^{99m}Tc, this product could be shipped to hospitals, allowing them to extract the daughter isotope for use in diagnostic imaging. The NRU was eventually shutdown due to its aging infrastructure, like many other reactors worldwide [10]. Infamous nuclear accidents, such as 3-Mile Island, Chernobyl, and the Fukushima Daiichi disaster, have resulted in a movement against nuclear power spreading throughout the world. These concerns, paired with economic and political factors, have resulted in large-scale reactor shutdowns. Nevertheless, industries around the world are starting to invest more time and money into this pursuit once again.

Cyclotrons have been used for isotope production since 1936, six years after the invention of a cyclotron [13]. However, with the rise of nuclear reactors in the mid-1900s, the usefulness of cyclotrons was diminishing. Canada's particle accelerator center, TRIUMF, proved the capabilities of cyclotrons in 1972, when it unveiled the world's largest cyclotron, 18 m in diameter with a 520 MeV beam [13]. Since then, many radioisotopes have shown great promise in being manufactured in cyclotrons such as TRIUMF's 13 MeV cyclotron in Vancouver, British Columbia. These radioisotopes include F^{18}, C^{11}, Ga^{68}, and Tc^{99m} [13]. The smaller size of cyclotrons also improves the accessibility of production, allowing hospitals and cancer clinics, such as BC Cancer Vancouver, to produce radioisotopes on-site. BC Cancer Vancouver has an ACSI TR-19 cyclotron, which fits in a single shielded room and is used for ^{18}F production [14].

1.3 Limitations of Radioisotope Production in Cyclotrons

Although cyclotrons pose a safer and cheaper alternative to radioisotope production than traditional reactor production, they can result in a low yield. The design of the cyclotron target, including the efficacy of the cooling design of the system, influences the thermodynamic conditions within the target. If not optimized, this can result in a low yield of the intended medical radioisotope product.

Cyclotrons accelerate a beam of ions in a spiral path until the beam is extracted and directed towards a target. This extraction process deposits a high-energy proton beam into the target chamber, rapidly heating the system. Depending on the energy of the beam and the effects of cooling across the system, boiling can occur in the liquid target chamber. As the water boils, a phase change occurs at 100 ° C, causing bubbles to appear in the chamber. These bubbles act as gaps, allowing the beam to travel through them and possibly hit the back wall of the target [11]. Due to this, less of the intended nuclear reaction occurs, and

overall, there is a lower yield of product.

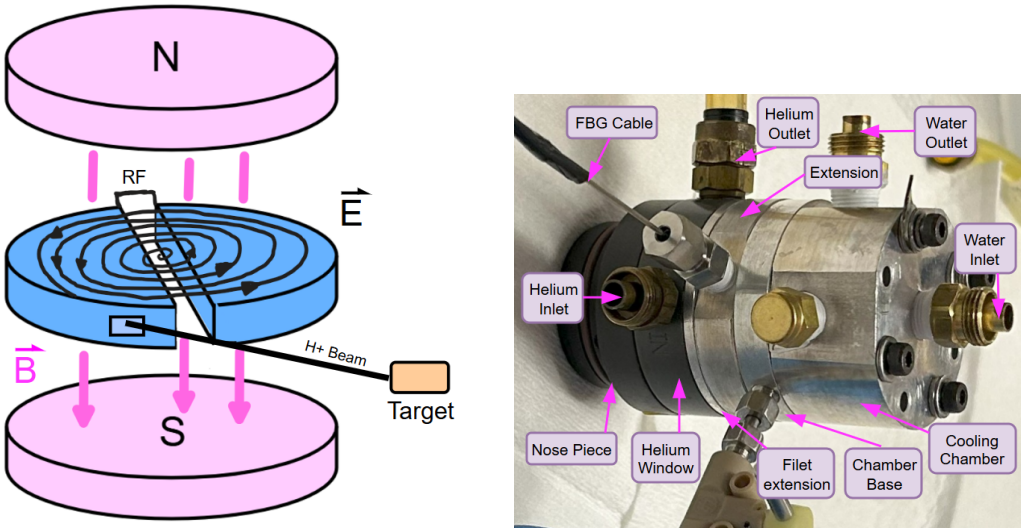

Figure 1.1: (A) Diagram of the workings of a cyclotron target. An RF system provides an alternating electric field, while a constant magnetic field is present. The ion beam travels in a spiral path until it is extracted and directed towards the target. (B) Liquid cyclotron target used to collect FBG temperature data upon being irradiated by TRIUMF's 13 MEV cyclotron [1].

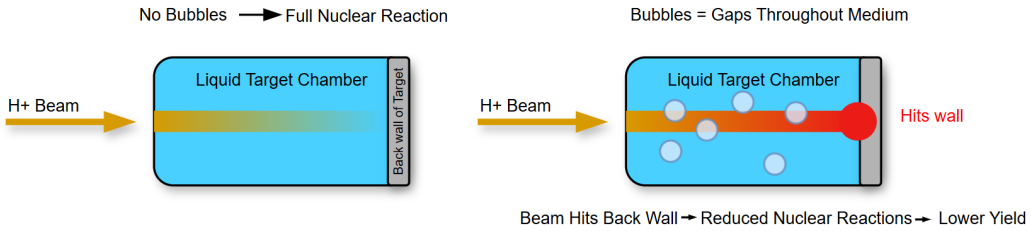

Figure 1.2: Diagram displaying the issue of low yields in liquid cyclotron targets as a result of their internal thermodynamic behaviour.

1.4 Motivation

A former Master's student at the University of British Columbia (Okanagan Campus) developed a technique to acquire real-time temperature readings of the liquid target chamber during irradiation [1]. Fibre Bragg Gratings (FBGs) were chosen as sensors to acquire temperature data due to their small size and resistance to environments possessing extreme pressure, temperature, and/or radiation conditions [12]. FBGs etched into a section of optical fibre can reflect a specific wavelength of light. As the fibre gets hotter due to increased temperature in the target environment from the irradiation, the fibre will expand, changing

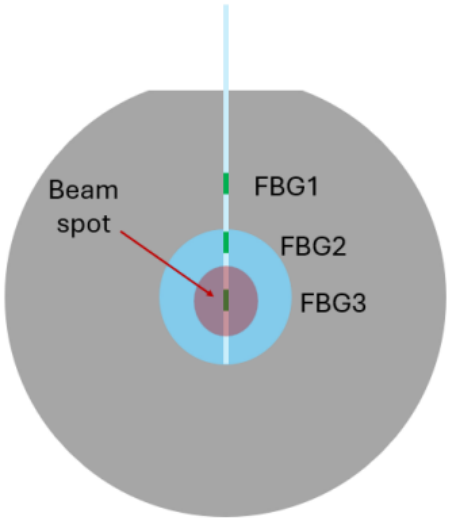

Figure 1.3: Positioning of FBG sensors within the liquid target [1].

its optical properties, and resulting in a different Bragg wavelength to be reflected. By measuring the reflected signal, the temperature of the FBG can be determined. Three FBG gratings were etched onto an optical fiber that was inserted into the target chamber cavity: FBG3 was a sensor at the center of the beam spot, FBG2 was at the edge of the target chamber, and FBG1 was within the aluminum cannister containing the chamber. The purpose of FBG1 was to monitor if heat was escaping from the target chamber into the cannister, as this could cause the o-ring seal keeping the system water-tight to fail.

Within solid and liquid targets, a temperature gradient exists. For solid targets, conduction is the cause; liquid targets are more complex, being influenced by radiolysis-driven convection of fluid [1]. The former student acquired temperature measurements inside liquid and solid cyclotron targets using FBGs as sensors [1]. This data confirmed the problem of boiling within high beam current irradiations and provided a set of thermal measurements to be used for the construction of computational models. For solid targets, ANSYS modelling was executed to determine a refined value for the helium heat transfer coefficient, h, and to replicate the observed thermal measurements [1].

1.5 Research Goal

The goal of this research was to replicate the previously acquired temperature measurements of the liquid target through computational thermal modelling. The model was produced using ANSYS to model the thermal distribution within a liquid target of TRIUMF's 13 MeV cyclotron. To achieve this, four objectives were pursued: creating a CAD model of the liquid target using SolidWorks (Student Edition 2025); using the Stopping and Range of Ions in Matter (SRIM) software (specifically the Transport of Ions in Matter (TRIM) program) to observe and understand the behaviour of the proton beam as it travels through the target; running thermal simulations in ANSYS using beam parameters provided

by TRIM to acquire modelled temperature data of the liquid target; and understanding and quantifying the limitations of the computational thermal model by determining the associated uncertainty.

By doing this modelling, it was determined whether or not the experimentally measured temperatures could be achieved, given the initial conditions of the system. The heat transfer coefficient (W/m^2K) for Helium was varied in an attempt to improve the agreement of the model with the observed thermal measurements.

Chapter 2

Methods

2.1 Software Overview

2.1.1 SolidWorks

SolidWorks is a widely used software for creating three-dimensional computer-aided design (CAD) files [15]. CAD files can then be used as blueprints for 3D printing, structural or electrical designs, or as part components to do computational modelling in other software programs. This license was acquired through the UVIC Engineering and Computer Science SolidWorks Engineering Kit (SEK).

2.1.2 Stopping Range of Ions in Matter (SRIM)

The Stopping and Range of Ions in Matter (SRIM) software was developed in the 1980s by James Ziegler [16]. It is a free-to-use but not open-source software commonly used in ion implantation research. Using a Monte-Carlo based approach, SRIM is able to simulate how ions lose energy during their passage through material. Input parameters include ion type and energy, as well as target materials. Output data includes ionization spread, ion penetration depth, and ion trajectories.

2.1.3 ANSYS

ANSYS is an engineering simulation software that is commonly used in industry [17]. Multiple ANSYS packages were used for this research. ANSYS Discovery and ANSYS SpaceClaim were used to make quick design adjustments and measure physical components of the system. ANSYS Mechanical was used to model steady-state thermal behaviour across structures, while ANSYS Fluent incorporated transient fluid flow throughout the system. ANSYS Workbench was used to integrate the CAD design, mesh, and solution parameters together in order to run the simulation and achieve results.

2.2 Building a CAD Model of the Liquid Target

SolidWorks 2025 - Student Edition was used to create a Computer-aided Design (CAD) model of the liquid cyclotron target. Draft drawings provided by TRIUMF were used to

construct the Fillet Chamber Extension, Target Chamber Base, and Target Cooling Chamber of the model. The Nose Piece and Helium window were designed for this project based on an image of the actual liquid target setup. The dimensions of these pieces were estimated relative to the sizes of the other components. The research of former UBCO Medical Physics Master's student, Grace Dehnel, provided the draft drawing needed for the Target Chamber Extension section of the model [1].

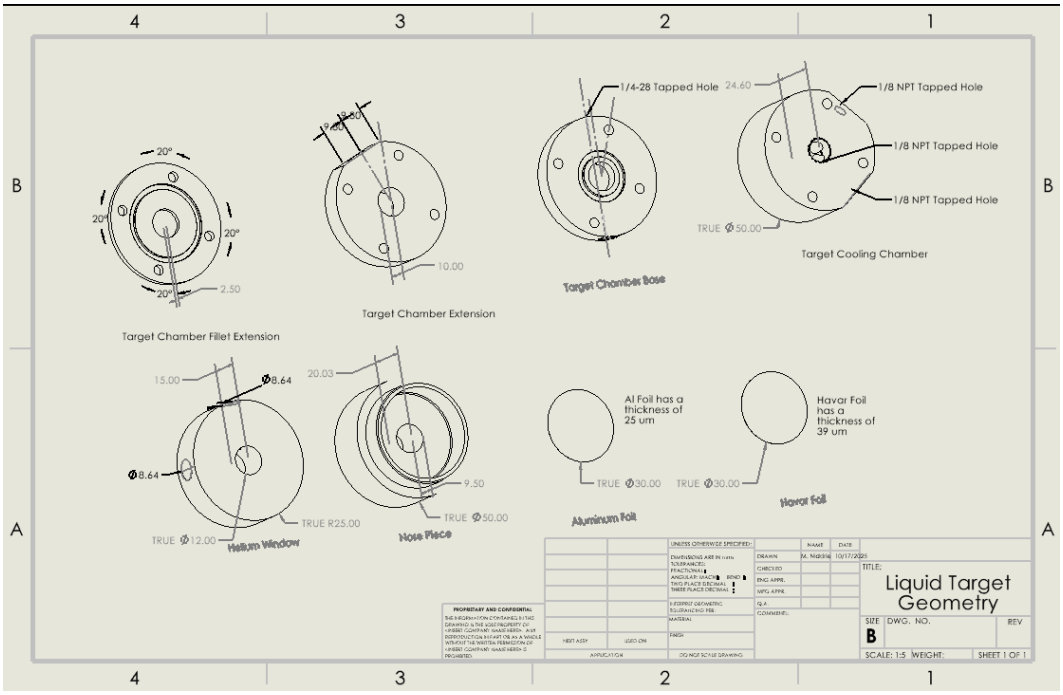

Figure 2.1: Sample of format of draft drawings used to create CAD model of the Liquid Target. Note: these are not actual TRIUMF draft drawings but were created by the author.

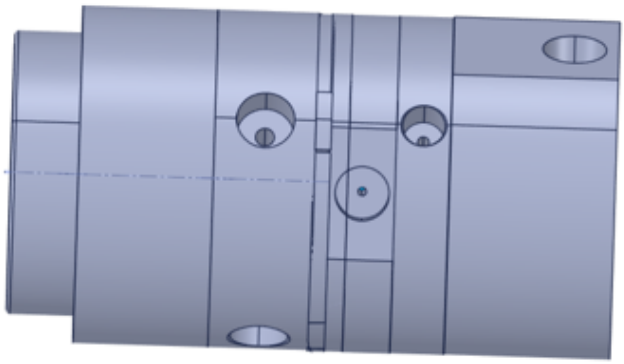

(a)

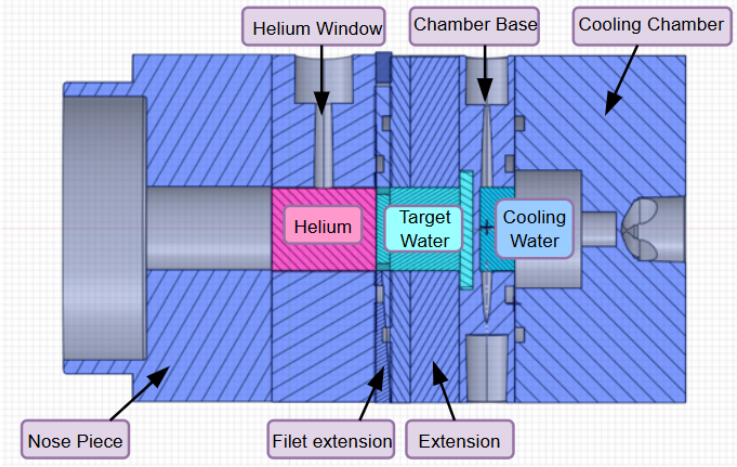

(b)

Figure 2.2: (A) SolidWorks CAD model of liquid target (B) Cross-sectional view of liquid target, light blue representing the target water volume, dark blue representing the cooling water volume and pink representing the helium coolant region.

During subsequent thermal modelling, any major changes to the CAD file were made using ANSYS Discovery or ANSYS Spaceclaim, as this allowed for real time mesh adaptations to the modifications.

2.3 Modelling the Passage of a 13 MeV H^+ Beam

To find thermal information for each section of the target, the passage of a 13 MeV proton beam was modelled. This beam travels through three major sections in the target: the Aluminum Window, the Havar Window, and the liquid target water chamber. Havar

is an alloy with an overall density of 8,300 kg/m^3, consisting mainly of Cobalt (42%), with smaller fractions of Chromium, Nickel, Tungsten and a few other various elements.

Table 2.1: Elemental composition of Havar alloy [19].

Element	**Composition (%)**
Cobalt (Co)	42.00
Chromium (Cr)	19.50
Iron (Fe)	19.05
Nickel (Ni)	12.70
Tungsten (W)	2.70
Molybdenum (Mo)	2.20
Manganese (Mn)	1.60
Carbon (C)	0.20
Beryllium (Be)	0.05

Table 2.2: Thermal properties of liquid target materials which encounter the beam [19]. Thermal conductivity is denoted as k.

Material	**Density (kg/m^3)**	**Melting Point (°C)**	**k (W/mK)**
Havar	8300	1480	13.000
Aluminium (Al)	2699	660	237.000
Water (H_2O)	1000	0	0.600
Helium (He)	125		0.150

This passage was modelled using the Stopping and Range of Ions in Matter (SRIM) software, specifically utilizing the Transport of Ions in Matter (TRIM) program. The software requires entering the target materials and their properties in the order in which the beam will encounter them. The significant properties included in this simulation were the width of the material layer, as well as the material density (g/cm^3). Since Havar is an alloy, it was created as a custom material for this simulation. This process involved manually entering the densities of each element present in Havar with their associated percent compositon.

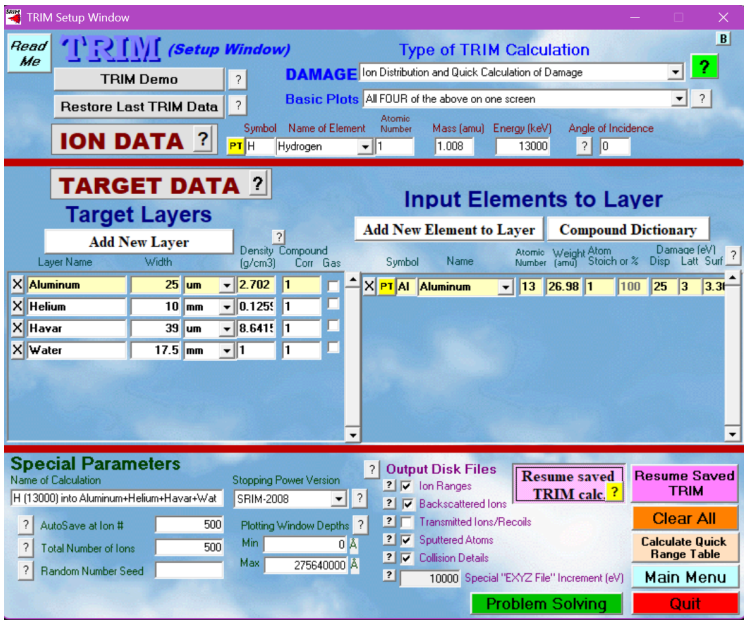

Figure 2.3: TRIM set up of a 13 MeV proton beam through Aluminium, Helium, Havar, and then water at specified thicknesses. The EXYZ file option was selected to create an ionization per depth file for future analysis.

An initial ion count of 500 ions was used to establish familiarity with the software and to produce baseline data. Due to Helium's low density and that it was being introduced only to cool the system, then immediately carried out, it was not included in the final TRIM runs that would be used to determine the energy deposited in each layer. SRIM runs were completed, including and excluding Helium, to observe the difference in the beam's energy loss as it travelled.

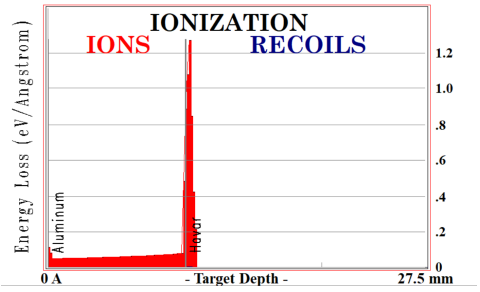

(a) He present

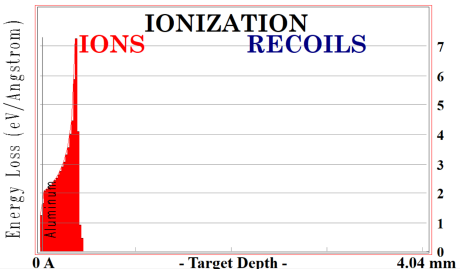

(b) No He

Figure 2.4: Sample SRIM output files displaying the energy loss to ionization of the ions in the beams, displaying the characteristic Bragg peak of a H^+ beam. The SRIM runs had the beam travel through (A) Al, He, Havar, and H_2O, and (B) Al, Havar, H_2O.

2.4 Determining the Power Deposited in Each Layer of the Liquid Target

One of the output files after a completed TRIM run is an EXYZ text file, which contains information about the ion energy loss as it travels through a material. This information is repeated for every ion in the run.

```
Calc. Date= 10-17-2025, Time= 21:06:27
============================== SRIM-2013.00 ==============================
 ==========================================================================
 =                   Ion Energy vs Position File                          =
 ==========================================================================
 =   AXIS DEFINITIONS: X=Depth, Y,Z= Lateral plane of target surface.=
 =   (If beam enters target at an angle, this tilt is in Y direction)=
 =   Shown are: Ion Number, Energy (keV), X, Y, Z Position            =
 ==================  CALCULATION   DATA  ============================
  Ion Data: Name, Mass,   Energy , Energy Interval
            H     001.01  13000keV    1000eV
 ==========================================================================
Ion       Energy     Depth (X)     Y           Z       Electronic   Energy Lost to
Number    (keV)    (Angstrom)  (Angstrom)  (Angstrom)  Stop.(eV/A)  Last Recoil(eV)
------- ---------- ---------- ----------- ----------- -----------  ---------------
0000001 1.3000E+04  0.0000E+00  0.0000E+00  0.0000E+00  7.4864E-01  0.0000E+00
0000001 1.2952E+04  5.7371E+04  2.2293E-02  6.5637E-02  7.5081E-01  2.3947E+00
0000001 1.2930E+04  9.5991E+04 -6.1828E+01  5.9722E+01  7.5183E-01  7.1232E-01
```

Figure 2.5: A sample EXYZ file. Significant columns are the Ion Number, Energy (keV), Depth X (Å), Y (Å) , and Z (Å). The lateral spread of the beam is described by the Y and Z coordinates.

The Python program `Pandas` was used to read into this file, extract data from specified columns, and then calculate the energy deposited in each layer. The associated Python code can be found in the Appendix. Each target material has a specific thickness, as determined by the dimensions of the model. For Al, the thickness was $25\mu m$, Havar 39 μm, and water 17.5 mm. The energy was found at the end of each layer through the following method:

Calculation 1. Finding the energies deposited into each target material, where al_energy, havar_energy, and water_energy were the energies of the beam at the far edge of each material.

$$\text{al\_deposited} = 13000\text{keV} - \text{al\_energy} = 192.00\text{keV}$$

$$\text{havar\_deposited} = \text{al\_energy} - \text{havar\_energy} = 841.00\text{keV}$$

$$\text{water\_deposited} = \text{havar\_energy} \ - \text{water\_energy} = 11966.01\text{keV}$$

The power deposited into each material was found by multiplying by the beam current (μA).

Calculation 2. Finding the power deposited into each target material, where I is the beam

current (μA), and E is the energy deposited (MeV).

$Q = IE$
$Q_{Al} = 1.5\mu A \times 0.192\text{MeV} = 0.288W$
$Q_{Havar} = 1.5\mu A \times 0.841\text{MeV} = 1.262W$
$Q_{H2O} = 1.5\mu A \times 11.966\text{MeV} = 17.949W$

2.5 Utilizing Measured FBG Temperature Data

Measured FBG temperatures were provided by Grace Dehnel's previous research utilizing Fibre Bragg Gratings (FBGs) as sensors during the irradiation of liquid targets [1].

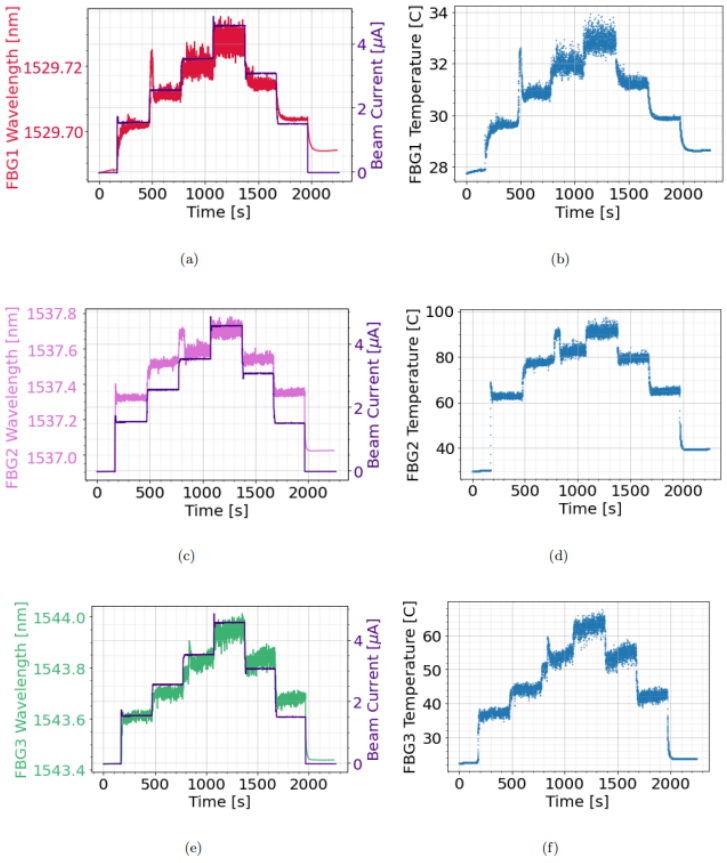

Figure 2.6: Measured FBG Data. From the FBG temperature data, specific temperatures were found for each beam current by interpolating at the midpoint of each temperature range. Associated uncertainties were found by taking the absolute difference of the maximum and minimum temperatures, then dividing by two. [1]

2.6 Thermal Modelling of Liquid Target Irradiation using ANSYS Mechanical

Each power value (W) was divided by the volume of the material to provide the volumetric heat source (W/m^3) needed for thermal modelling. These volumetric heat sources generated the heat across the model, while cooling was provided by a Helium volume at 22° C and a Water volume at 20° C [1] [23]. It should be noted that these inlet temperatures of the Helium and water coolant volumes were assumed from literature rather than being measured directly [1] [23]. As a result, conservative uncertainty estimates of ±4° C and ±2° C, for Helium and water, respectively, may introduce additional error beyond what is reported in the simulation results of this paper.

ANSYS Mechanical was used to simplify the model, treating fluid objects as static masses with no fluid dynamics. This was done to see if the modelled temperature could get within the range of temperature measurements, even with simplifications to the Physics.

After importing the CAD file of the target into ANSYS Workbench, a steady-state thermal simulation cell was created, and materials were selected to include in the simulation. Mechanical was opened, and these materials (Aluminum, Havar, Water, and Helium) were assigned to their respective volumes. To establish the heat sinks, cooling through convection was assigned to the Helium and Water coolant regions. Helium's heat transfer coefficient, h, is not well known. Previous research found that a value of 875 W/m^2K accurately modelled observed temperatures in solid targets, so this value was used as a starting point for liquid target simulations [1]. This h-value of 875 W/m^{2}K and a temperature of 22° C was assigned to the Helium volume, creating a heat sink. The same process was applied to the cooling water, with a h-value of 10000 W/m^2K and an ambient temperature of 20°c.

The previously calculated volumetric heat sources (W/m^3) were assigned to 10 mm diameter regions of the volumes of Aluminum, Havar, and Water. To help simulate the effects of the Bragg peak of water, water's volumetric heat source term was restricted to the first 2.5 mm depth of the water volume instead of covering the full 17.5 mm depth. The first 2.5 mm was selected considering the behaviour of the Bragg peak as seen in Figure 2.4 and 3.1.

Running the thermal simulation generated temperature contour curves across the target, with red being hotter temperatures and blue being cooler temperatures. Temperature probes were used to see the modelled temperature at the location of the FBG sensors. The maximum and minimum temperatures across the entire system were also probed.

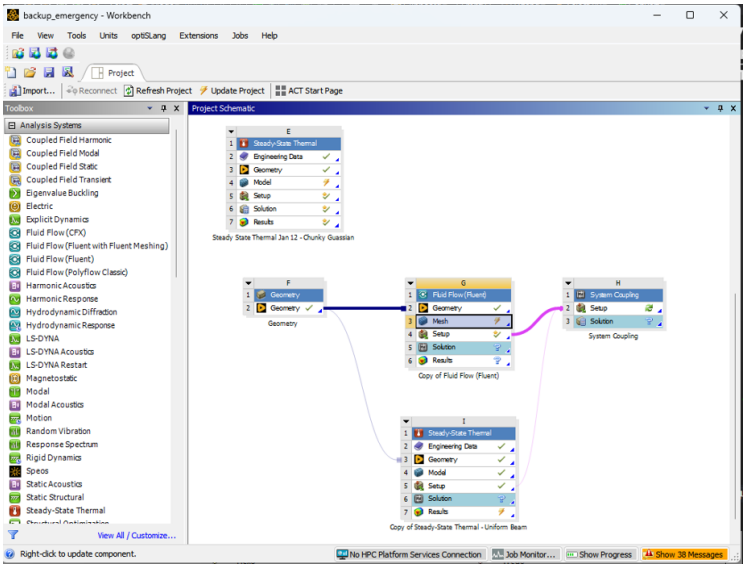

Figure 2.8: ANSYS Workbench sample setup for a Steady State Thermal run through ANSYS Mechanical. Below, a more complicated setup method is displayed, attempting to connect ANSYS Fluent and ANSYS Mechanical simulations together. This second setup method is included to display how ANSYS Workbench can be used to combine results from multiple simulations, as well as have them feed into each other, affecting their results.

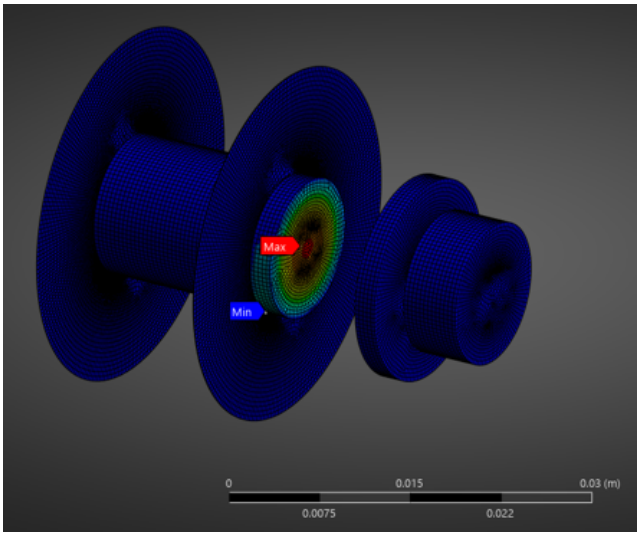

Figure 2.7: Temperature contour curves displayed on specific sections of the liquid target. Blue represents cooler temperatures, with the transition to red representing hotter temperatures.

2.7 Thermal Modelling of Liquid Target Irradiation using ANSYS Fluent

ANSYS Fluent was used to improve upon the limitations of the ANSYS mechanical model, allowing for proper convection of fluid across the system. To capture the flow behaviour of the fluids present, Fluent uses the Finite Volume Method (FVM) which breaks the mesh up into small cubical volumes, allowing for proper modelling of fluid flow.

Due to the size of the Havar and Aluminum windows (0.39 μm, and 0.25 μm thick, respectively), the FVM would need to significantly increase the mesh resolution from the previous element size of 4×10^{-4} m in order to resolve these small features. This would greatly increase the simulation time and possibly contribute to errors across the model. To account for the heat generated across these windows, thermal "wall" boundary conditions were applied at the interfaces between the helium and target water, helium and environment, and target water and cooling water regions. These walls were assigned a specified thickness and material properties corresponding to the Aluminum and Havar windows, with the beam flux density, φ, applied at the appropriate locations.

$$\varphi = \frac{Q}{\sigma}$$

where Q is the power generated in the region, and σ is the cross-sectional area of the interface. This approach captures both the heat generation at the windows and the heat transfer through them, while avoiding the meshing issues associated with modelling the very thin solid geometries of the windows. Helium and coolant water were added to their respective volumes in the system, entering from a velocity inlet and exiting from a pressure outlet. This behaviour mirrors the setup of the actual liquid target.

The first 2.5 mm of the target water region, with a 10 mm diameter, was assigned an energy source term (W/m^3), this value, along with the flux densities (W/m^2) of the Havar and Aluminum windows, was altered during different beam current simulations.

The Boussinesq approximation was applied to water containing regions, which allowed for modelling of buoyancy-driven fluid flow.

$$\rho g_i \approx \rho_0 \left[1 - \beta(T - T_0)\right] g_i \tag{2.1}$$

where ρ_0 is the reference density (set to 998.21 kg/m^3 for water), β is the thermal expansion coefficient, T is the local fluid temperature, and T_0 is the reference temperature (set to 20° C) [21].

To model the viscosity of the fluids, a STS k-ω turbulence model was used to approximate the Reynolds-averaged Navier–Stokes equations. It predicts the turbulent kinetic energy, k, and the rate of dissipation, ω.

The Reynolds-Averaged Navier-Stokes (RANS) momentum equation is given by [20]:

$$\rho \bar{u}_j \frac{\partial \bar{u}_i}{\partial x_j} = \rho \bar{f}_i + \frac{\partial}{\partial x_j}\left[-\bar{p}\delta_{ij} + \mu\left(\frac{\partial \bar{u}_i}{\partial x_j} + \frac{\partial \bar{u}_j}{\partial x_i}\right) - \rho\overline{u_i' u_j'}\right] \tag{2.2}$$

where ρ is the fluid density, $\bar{u}_i$ and $\bar{u}_j$ are the mean velocity components, $\bar{f}_i$ is the mean body force per unit mass, $\bar{p}$ is the mean pressure, δ_{ij} is the Kronecker delta, μ is the dynamic viscosity, and $-\rho\overline{u'_i u'_j}$ is the Reynolds stress tensor, representing the effect of turbulent velocity fluctuations on the mean flow field [20].

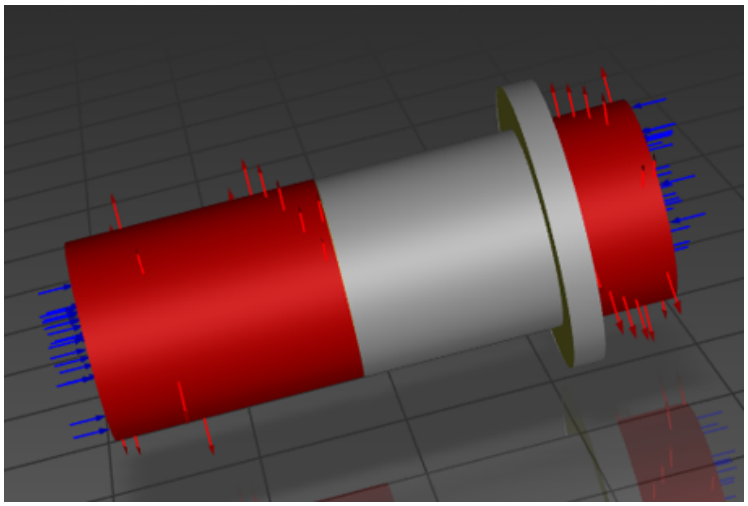

Figure 2.9: ANSYS Fluent simulation setup. Red arrows indicate coolant pressure outlets and blue arrows indicate coolant velocity inlets. Only the fluid bodies are shown, as the thin solid Havar and Aluminum windows produced mesh errors that could not be resolved.

Chapter 3

Results and Discussion

3.1 SRIM/TRIM Beam Modelling Results

It was found that the maximum energy deposition event occurred just after the Havar Window. From this, it can be said that the H^+ beam delivers a significant fraction of its energy to a small volume of water in the target. The ionization path found was in agreement with the expected Bragg peak behaviour of proton beams. The lateral spread of the proton beam could be displayed by plotting the Y (Å) and Z(Å) columns of the EXYZ file. This result shows that the beam is more concentrated in the center, as expected for a Gaussian Beam. In reality, ion beams do not display true Gaussian behaviour. As a result, running thermal simulations under the Gaussian assumption may lead to deviations from actual temperature measurements.

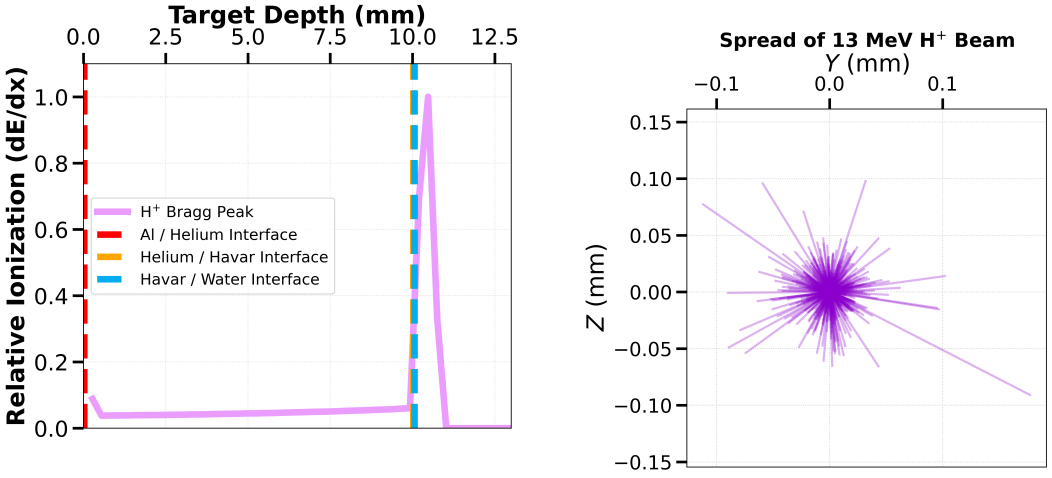

Figure 3.1: (A) Energy loss due to ionization of the 13 MeV H^+ beam as it travels through Al, He, Havar, and H_2O. (B) Lateral Spread of a 13 MeV H^+ beam.

From the TRIM `EXYZ` output file, the energy deposited in each cylindrical volume was found. Utilizing the beam current (μA) of each run, the power, and as a result heat

generation functions, could be found.

Table 3.1: Energy deposited in each material region by a 13 MeV proton beam.

Material	**Energy Deposited (MeV)**
Aluminium (Al)	0.192
Havar	1.215
Water	17.949

Table 3.2: Power generated in each material region at various beam currents by a 13 MeV proton beam.

Beam Current (μA)	**Al (W)**	**Havar (W)**	**Water (W)**
1.5	0.288	1.215	17.949
2.5	0.480	2.025	29.915
3.0	0.576	2.430	35.898
3.5	0.672	2.835	41.881
4.5	0.864	3.645	53.847

Table 3.3: Heat generation functions assigned to specified material volumes at various beam currents.

Beam Current (μA)	**Al (W/m^3)**	**Havar (W/m^3)**	**Water (W/m^3)**
1.5	$1.466\,768\,5 \times 10^8$	$3.966\,634\,0 \times 10^8$	$9.141\,35 \times 10^7$
2.5	$2.444\,614\,0 \times 10^8$	$6.611\,057\,6 \times 10^8$	$1.523\,558 \times 10^8$
3.0	$2.933\,537\,1 \times 10^8$	$7.933\,269\,7 \times 10^8$	$1.828\,270\,1 \times 10^8$
3.5	$3.422\,459\,9 \times 10^8$	$9.255\,480\,6 \times 10^8$	$2.132\,981\,82 \times 10^8$
4.5	$4.400\,305\,0 \times 10^8$	$1.189\,990\,36 \times 10^9$	$2.742\,405\,2 \times 10^8$

3.2 Comparing Modelled and Measured FBG Temperatures using ANSYS Mechanical

These simulation results show that natural convection-driven flow inside the liquid target chamber does not occur in ANSYS mechanical simulations. Heat sinks through convection were assigned at the Helium coolant and water coolant regions; however, this convection only occurred at the boundaries of the cooling surfaces and did not generate fluid flow across the system. As a result, the model did not accurately replicate the measured temperature measurements. Overlap in the measured (black) and modelled (pink) error bars indicates successful modelling; this overlap was not present in this model.

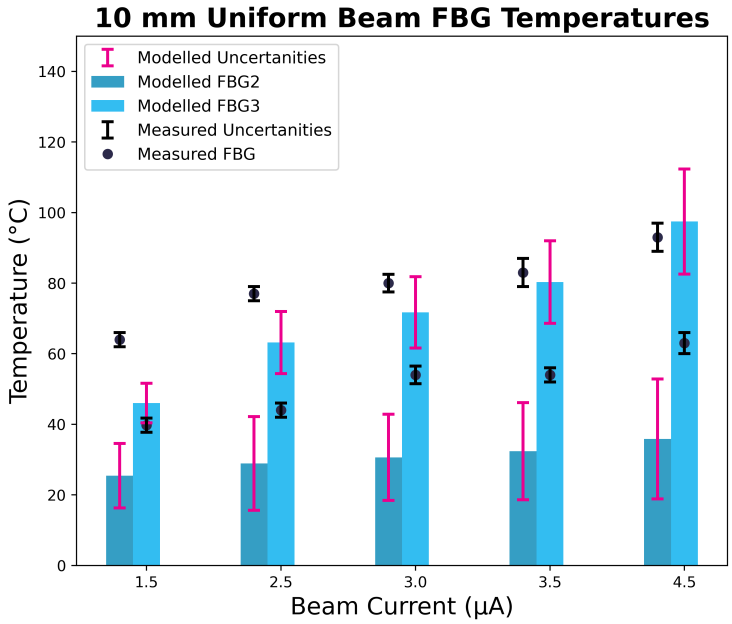

Figure 3.2: Measured and modelled temperature values at each FBG position for Helium's Heat Transfer Coefficient, h, set to h = 875 W/m^{2}K [1]. Uncertainty equations are shown below, Calculation 4 for the modelled thermal data, and Calculation 3 for the measured thermal data.

The black error bars represent the uncertainty in the measured temperature values, arising from the spread of temperatures detected by the FBG sensor at the given beam current. The maximum and minimum temperature values were manually interpolated from the FBG wavelength to temperature plots, as seen in Figure 2.6, generated by the former UBCO Master's student [1]. This process was repeated for every FBG sensor for every beam current (1.5, 2.5, 3.0, 3.5, 4.5) μA, allowing for the generation of the measured temperature data set.

Calculation 3. Associated uncertainity for measured FBG temperature data [1].

$$\delta T_{measured} = \frac{|T_{max} - T_{min}|}{2}$$

Table 3.4: Interpolated values for the measured temperatures at each FBG position for beam currents plus found uncertainties [1].

Beam Current (μA)	**FBG 1 (°C)**	**FBG 2 (°C)**	**FBG 3 (°C)**
1.5	29.85±0.2	64±2	39.75±2.0
2.5	30.90±0.2	77±2	44.00±2.0
3.0	31.40±0.3	80±2.5	54.00±2.5
3.5	32.00±0.7	83±4.0	54.00±2.0
4.5	32.90±0.9	92±4.0	63.00±3.0

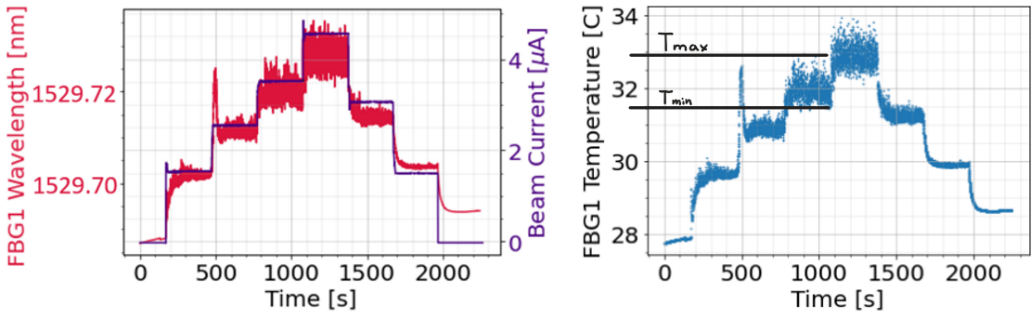

Figure 3.3: Method for determining $T_{measured}$ at a beam current of 3.5 μA.

To determine the uncertainty of the ANSYS model (pink error bars), factors that could directly impact the quality were considered, as seen in Calculation 4. These factors include positional sensitivity of the beam, quality of the mesh, noise in the system, and the impacts of Helium cooling, as Helium has a variable Heat Transfer Coefficient, h (W/m^2K).

Calculation 4. Associated uncertainty for modelled FBG temperature data.

$$\delta T_{model} = \sqrt{\delta T_{sa}^2 + \delta T_{noise}^2 + \delta T_{mesh}^2 + RSS_{min}^2}$$

The positional sensitivity, δT_{sa}, is relevant to the uncertainty of the exact placement of individual elements in the model, as well as uncertainty in the lateral position of the beam during the irradiation. The irradiated water region was selected to be shifted for the analysis, as the majority of the beam energy is deposited into this region. This allows for misalignments in the beam to be translated into the model. $T_{baseposition}$ represents the original position of the irradiated water volume, and $T_{adjusted}$ is the misaligned position.

Calculation 6. Defining δT_{sa}, which is the uncertainty in the temperature from the positional uncertainty across the model.

$$T_{sa} = \sqrt{\sum (T_{baseposition} - T_{adjusted})^2}$$

This process was repeated for each beam current; overall positional uncertainty results can be seen as Table 3.5.

Table 3.5: Positional sensitivity analysis results.

Beam Current (μA)	δT_{sa} **FBG 3 (°C)**	δT_{sa} **FBG 2 (°C)**
1.5	4.93	2.02
2.5	8.63	3.41
3.0	4.24	3.03
3.5	4.94	3.53
4.5	6.31	4.52

In TRIM, a finite number of ions was used to determine the energy deposited in each region of the model. This number started as 500 ions and was then increased to 10000 ions. This influences the possibility of noise in the model due to random temperature fluctuations from a limited number of particles. Increasing the number of particles helps to minimize the noise resulting from these fluctuations, improving the statistical reliability of the deposited energy distribution.

Calculation 7. Defining δT_{noise}, which is the uncertainty in the temperature from the initial temperature rise in the model due to noise in the system. N = the number of ions, and the ambient temperature is 20°C. The maximum temperature is the maximum temperature across the entire system at a specified beam current (μA).

$$\delta T_{noise} = \frac{1}{\sqrt{N}} \times (T_{max} - T_{ambient})$$

Table 3.6: Uncertainty resulting from noise in the system analysis results.

Beam Current (μA)	δT_{noise} **FBG 3 (°C)**	δT_{noise} **FBG 2 (°C)**
1.5	1.55	0.68
2.5	2.63	1.19
3.0	3.17	1.44
3.5	3.72	1.70
4.5	4.58	2.10

To run the thermal simulations using ANSYS, a less-than-ideal mesh was used, as this gave compilation output in a reasonable amount of time. The impacts of using a coarser, less-than-ideal mesh were investigated by comparing the temperature at each FBG sensor between a coarse mesh simulation and a fine mesh simulation.

Calculation 8. Defining δT_{mesh}, which is the uncertainty in the temperature due to temperature differences at different mesh sizes (coarse versus fine).

$$\delta T_{mesh} = |T_{coarse} - T_{fine}|$$

Table 3.7: Uncertainty in the mesh of the model analysis results.

δT_{mesh} **FBG 3 (°C)**	δT_{mesh} **FBG 2 (°C)**
5.96	2.35

To address the impacts of Helium cooling on the system, the effects of varying Helium's Heat Transfer Coefficient, h, were investigated.

Calculation 9. Defining RSS_{min}, which is the best fit value between the modelled and measured FBG temperatures found by adjusting the value of h.

$$RSS = \sqrt{\sum (FBGx_{model} - FBGx_{measured})^2};$$
$$\text{where } x = 2, \text{or } 3$$

Table 3.8: Uncertainty resulting from Helium's heat transfer coefficient, h, results.

Beam Current (μA)	**RSS**
1.5	4.62
2.5	7.70
3.0	9.24
3.5	10.78
4.5	13.86

From Calculation 4, the overall uncertainty in the model was found and can be seen in Table 3.5.

Table 3.9: Overall δT_{model} at each beam current for each FBG.

Beam Current (μA)	**FBG 3 (°C)**	**FBG 2 (°C)**
1.5	9.14	5.60
2.5	13.27	8.82
3.0	12.20	10.11
3.5	13.78	11.71
4.5	16.98	14.91

3.2.1 Creating an Approximate Gaussian Beam

As an ion beam travels down the beam line, its shape is not uniform laterally across the entire chamber, but instead it can be approximated as peaking at the center and radially dissipating outward. In previous simulations, a 10 mm diameter uniform beam volume was used. It was tested to see what effect breaking this beam up into small radial segments, each with energy decreasing from the center, would have. Although in reality, ion beams do not display true Gaussian behaviour, this method is a closer approximation than the previous 10 mm uniform beam approximation.

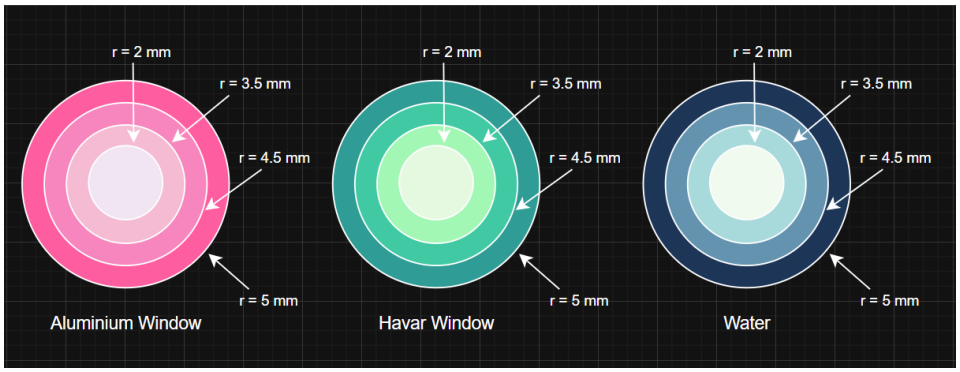

Figure 3.4: Aluminum, Havar, and heated Water regions broken up into rough Gaussian segments (r= 2, 3.5, 4.5, and 5 mm).

To distribute the deposited beam energy radially according to the Gaussian beam profile, the fraction of energy deposited in annular ring i, bounded by $r_{\text{in},i}$ and $r_{\text{out},i}$, was calculated using the cumulative Gaussian distribution:

$$f_i = e^{-r_{\text{in},i}^2/2\sigma^2} - e^{-r_{\text{out},i}^2/2\sigma^2}$$

where $\sigma = 1.5\,\text{mm}$ is the Gaussian beam width parameter. The energy deposited in ring i is then:

$$E_i = E_{\text{total}} \times f_i$$

and the corresponding power deposited in ring i at beam current I is:

$$P_i = \frac{E_i \times I}{1000}$$

where the factor of 10^{-3} converts E_i from keV to MeV, and I is the beam current in μA. This was evaluated for four concentric rings with boundaries at $r = 0$, 2, 3.5, 4.5, and 5 mm, for Aluminium, Havar, and Water at each beam current.

Table 3.10: Energy deposition per concentric ring for each layer of material, determined at specific radii boundaries.

Radius (mm)	**Al (MeV)**	**Havar (MeV)**	**Water (MeV)**
2.0	113.066	495.255	7046.636
3.5	66.314	290.468	4132.866
4.5	10.487	45.935	653.578
5.0	1.391	6.091	86.671

The data table for a beam current of 1.5 μA is included; however, the remaining data tables can be found in Appendix A. The total sum of the power generated throughout each ring nearly matches the total power of the 10 m uniform beam previously calculated. Determining the heat generation values required dividing each power by the ring volume; however, due to time constraints, this method was replaced by a faster approach that directly applied

Table 3.11: Power deposited per annular ring region in each material at 1.5 μA (inner to outer).

Ring	**Al (W)**	**Havar (W)**	**Water (W)**
Inner	0.1696	0.7429	10.5700
Ring 1	0.0995	0.4357	6.1993
Ring 2	0.0157	0.0689	0.9804
Ring 3	0.0021	0.0091	0.1300
Total	0.2869	1.2566	17.8797

a Gaussian approximation to the peak heat generation value.

The peak heat generation q_0^{peak} of the Gaussian was determined by requiring that the power integrated over the beam cross-section equals the total power deposited in each material:

$$P_{\text{total}} = \int_0^R q_0^{\text{peak}}\, e^{-r^2/2\sigma^2} \cdot 2\pi r\, dr \cdot t = 2\pi\sigma^2 t\, q_0^{\text{peak}} \left(1 - e^{-R^2/2\sigma^2}\right)$$

Solving for the peak value:

$$q_0^{\text{peak}} = \frac{P_{\text{total}}}{2\pi\sigma^2 t \left(1 - e^{-R^2/2\sigma^2}\right)}$$

where P_{total} (W) is the total power deposited in the material, σ is the Gaussian beam width, R is the beam radius, and t is the material thickness.

Assuming that the proton beam deposits energy following a Gaussian radial profile, with a beam width parameter of $\sigma = 1.5\,\text{mm}$, heat generation functions for each concentric ring could be found. For each material region, the average volumetric heat generation in ring i, bounded by $r_{\text{in},i}$ and $r_{\text{out},i}$, was calculated as:

$$\bar{q}_i = \frac{2q_0^{peak}\sigma^2 \left(e^{-r_{\text{in},i}^2/2\sigma^2} - e^{-r_{\text{out},i}^2/2\sigma^2}\right)}{r_{\text{out},i}^2 - r_{\text{in},i}^2}$$

where q_0^{peak} (W/m^3) is the peak volumetric heat generation at the beam center for each material, and $r_{\text{in},i}$, $r_{\text{out},i}$ are the inner and outer radii of ring i respectively.

In SolidWorks, concentric rings and an inner circle could be created from the original 10 mm beam using the Split Object tool. When imported back into ANSYS, heat generation functions could be assigned to each of these new volumes. It was found that using this method, no improvement in the FBG temperatures was observed across the system.

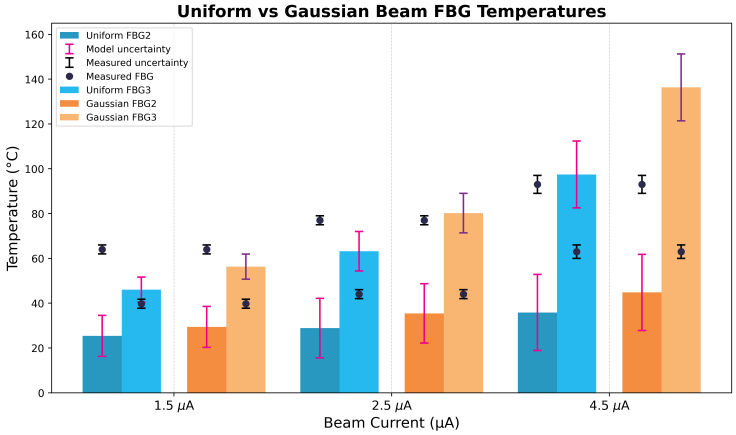

Figure 3.5: A comparison of measured and modelled temperature values at each FBG position for uniform 10 mm beam versus a rough Gaussian beam (Helium's Heat Transfer Coefficient, h, set to h = 875 W/m^{2}K) [1].

In the future, the original method of creating a rough Gaussian should be applied to the simulation to allow for comparison between the two methods.

3.3 Effects of Adjusting Helium's Heat Transfer Coefficient, h (W/m^{2}K)

Adjusting Helium's heat transfer coefficient, h, had little effect on the temperatures at the FBG probe positions. The impact of altering the h value was quantified by comparing the Residual Sum Square (RSS) values of multiple iterations.

$$\text{RSS} = \sum_{i=1}^{n} (y_{model} - y_{measured})^2$$

The RSS represents the error between the modelled and measured values, the h value that minimized the RSS provided the best fit to the system. The associated RSS$_{min}$ was included in the modelled uncertainity.

When plotting the RSS of the beam currents against the heat transfer coefficient, an interesting trend was found. The optimal h value for a beam current of 1.5 μA was 750 W/m^{2}K, but at 2.5 μA the optimal value was 1050 W/m^{2}K. The trend for the lower beam current, 1.5 μA, was that the RSS increased as h increased. However, for 2.5 μA, the opposite trend was shown; the RSS decreased as h increased.

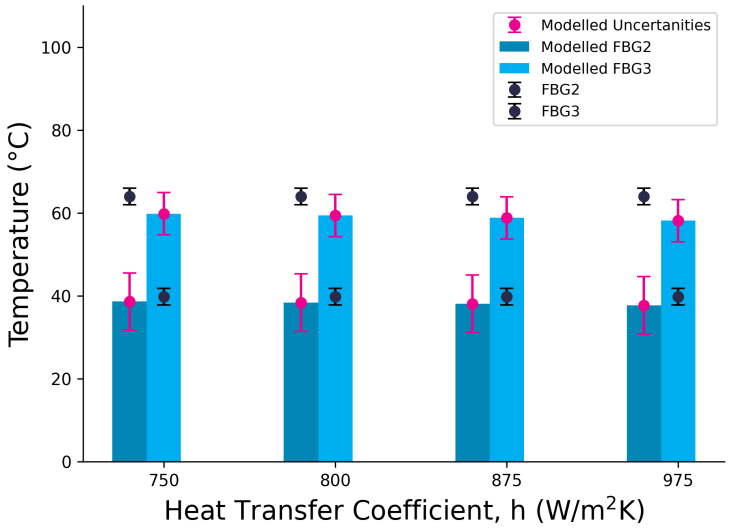

(a)

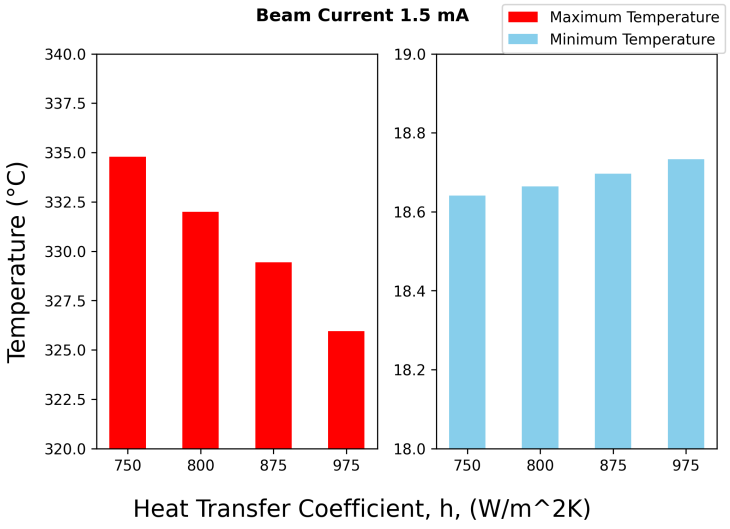

(b)

Figure 3.6: Effects of adjusting Helium's Heat Transfer Coefficient, h (W/m^{2}K), on the model at a constant beam current of 1.5 μA at the (a) FBG sensors, (b) maximum and minimum temperatures across the model.

Table 3.12: Implications of altering Helium's heat transfer coefficient, h (W/m^{2}K), on the thermal model for beam currents of 1.5 μA and 2.5 μA.

He h Value	**Beam Current (μA)**	**FBG 3 (°C)**	**FBG 2 (°C)**	**RSS**
750	1.5	59.805	38.586	4.53
800	1.5	59.377	38.360	5.01
875	1.5	58.797	38.052	5.68
975	1.5	58.119	37.692	6.46
750	2.5	86.192	50.861	11.95
875	2.5	84.503	49.962	10.01
975	2.5	83.366	49.356	8.71
1050	2.5	82.612	48.953	7.86

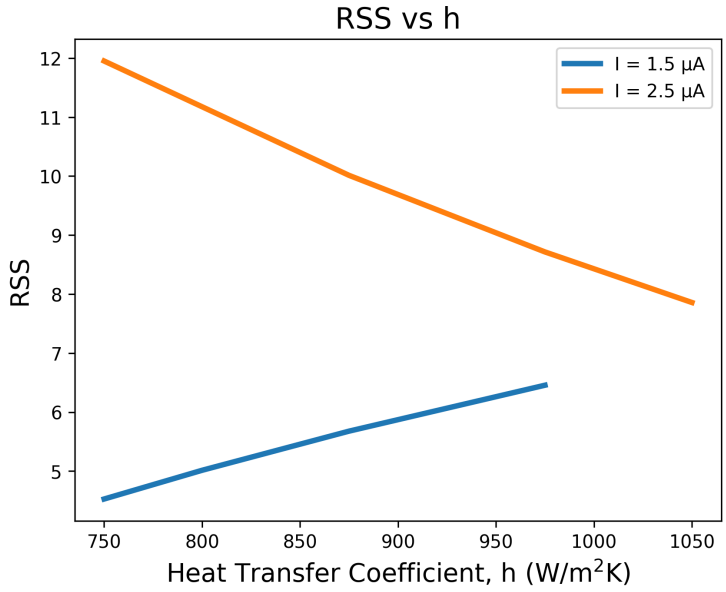

Figure 3.7: Viewing how the RSS changes for various heat transfer coefficient values at beam currents of 1.5 μA and 2.5 μA.

The heat transfer coefficient, h, represents the rate of convective heat transfer between a fluid, here the Helium, and a solid, here the havar window. A higher heat transfer coefficient indicates that heat from the target chamber is able to travel more efficiently into the Helium coolant. For a beam current of 1.5 μA, increasing h could lead to overcooling in the model, causing the RSS value to increase as the model deviates from the measured temperatures.

At higher beam currents, more heat is generated across the system. Heat from the havar window could result in nucleate boiling. When water exposed to a surface that is at a temperature a few degrees greater than the saturation temperature (100° C for water), small isolated bubbles begin to form at the interface [18]. When these small bubbles move

to the center of the target, which is cooler, they collapse [18]. This mechanism allows heat to be carried away from the havar window. The ANSYS Mechanical simulations did not account for bubbles or phase changes occurring in the system, as no flow or multiphase settings were applied to the model. This is why for higher beam currents, the model was only optimized when the value of h was increased. In this situation, the model would use a fake h solely to account for the bubble cooling effect. To test this theory, the Havar surface temperature predicted by the model at each beam current should be examined. If nucleate boiling is the mechanism causing the difference in RSS, the Havar surface temperature should approach or exceed 100°C at 2.5 μA but remain below this threshold at 1.5 μA.

Due to a lack of time, the impacts of adjusting h (W/m^2K) at each beam current could not be explored. An approximation was used to apply an estimate of the RSS value at higher beam currents to the modelled data. At 1.5 μA, the RSS that optimized the model was 4.53, while for 2.5 μA it was 7.86. Under the assumption that the nucleate boiling effect would intensify as the applied beam current increased, the deviation between the ANSYS Mechanical model and the measured temperatures would grow correspondingly. The model does not account for the additional heat transfer carried away by bubble collapse, meaning the gap between modelled and measured temperatures widens as the boiling contribution becomes more significant. The RSS is a direct measure of this deviation, and is therefore expected to increase with beam current. Using the two optimized RSS values, an approximate RSS per unit beam current was calculated and applied to estimate the model uncertainty at higher beam currents, as shown in Calculation 10.

Calculation 10. Finding the RSS at higher beam currents.

$$
\begin{aligned}
4.53/1.5\mu A &= 3.02\ (\text{RSS})/\mu A \\
7.86/2.5\mu A &= 3.14\ (\text{RSS})/\mu A \\
\text{Average } &= 3.08\ (\text{RSS})/\mu A \\
\text{Multiplying by the beam current } (\mu A):& \\
3.0\mu A &\rightarrow 9.24 \\
3.5\mu A &\rightarrow 10.78 \\
4.5\mu A &\rightarrow 13.86
\end{aligned}
$$

These values should be treated as conservative estimates rather than precise quantities, as the exact optimal h (W/m^2K) value at each higher beam current was not determined.

3.4 Positional Sensitivity Analysis

Adjusting the position of the irradiated target water volume in the system displayed sensitivity in the model, leading to temperature discrepancies. The process of the sensitivity analysis involved incrementally shifting the irradiated target water volume at a maximum depth of 2.5 mm in the z-direction (perpendicular to the beam path). The beam current (μA), as well as the energy deposited in the aluminum window, Havar window, and irradiated water, were kept constant. For each run of this analysis, the temperature was recorded at each FBG position, as well as the maximum and minimum temperatures of the system.

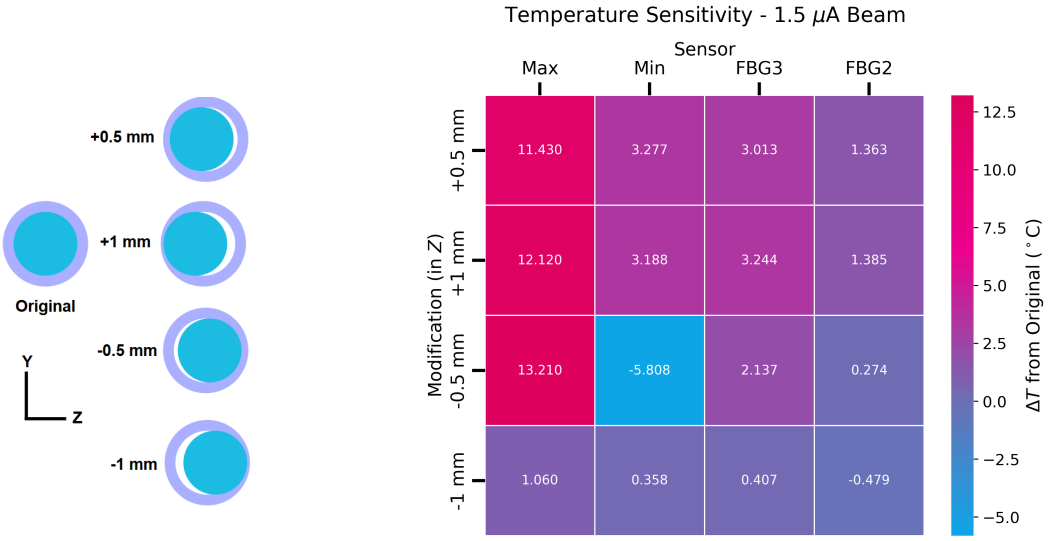

Figure 3.8: Positionally dependent temperature sensitivity analysis for a beam current of 1.5 μA after moving an irradiated water region 0.5 mm and 1 mm in the positive and negative z-direction. The diagram displaying the misalignment in the model is not to scale and is included as a visual representation of the process.

Data was plotted as heat maps relative to the original position of the irradiated water region, allowing the temperature change from the original position to be observed visually (Figure 3.12, 3.13).

For each beam current (1.5, 2.5, 3, 3.5, 4.5) μA, even slight misalignments across the system resulted in noticeable effects in the temperature at the sensors. The maximum and minimum temperatures of the system were the most impacted by the misalignments. These misalignments resulted in gaps forming between the target water and the target chamber walls. As a result, connectivity fails at that interface, causing a buildup of heat on one side of the gap, while the other side of the gap appears colder.

The impacts of rotating the irradiated water region by 90° were investigated, resulting in large temperature changes in the maximum temperature across the system. If the cylindrical irradiated water volume rotates from its edge instead of its axis, the heat distribution becomes non-uniform. This happens because the cylinder swings away from parts of the target, leaving them unexposed. Additionally, having the cylindrical volume not be exactly centered within the chamber could result in gaps forming when rotated on axis. Both rotation methods could have resulted in connectivity issues throughout the model, causing some sides of the irradiated water to not be exposed to coolant.

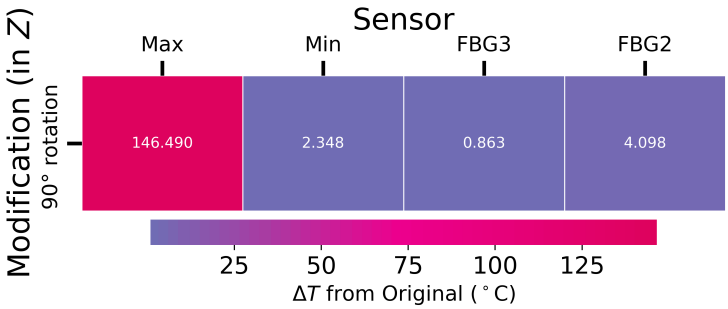

Figure 3.9: Positionally dependent temperature sensitivity analysis for a beam current of 1.5 μA after rotating an irradiated water region by 90° in the zy plane.

This analysis does not account for a second form of positional sensitivity: angular uncertainty in the incoming beam's transverse directions. Since the beam angular trajectory at the target entrance is adjusted by cyclotron parameter settings or target tilting mechanisms, its trajectory may not be perfectly perpendicular to the target face. These simulations assume a direct, perpendicular impact of the beam. To improve the positional sensitivity analysis in the future, angular uncertainties in the transverse directions should be explored.

3.5 Comparing Modelled and Measured FBG Temperatures using ANSYS Fluent

To test different model variations, it was viewed how the system would respond during transient second-order implicit simulations. Steady state simulations were not used here, as they would calculate the equilibrium conditions of the system. During the irradiations, as seen in Figure 2.6, each beam current ran for around 300 s before moving to the next beam current [1]. The need for time-accurate physics prompted the decision to run transient simulations, allowing the user to incrementally increase the simulation length. This process allowed the user to watch the temperature distribution of the target as increasing quantities of hot water rose to the top of the chamber.

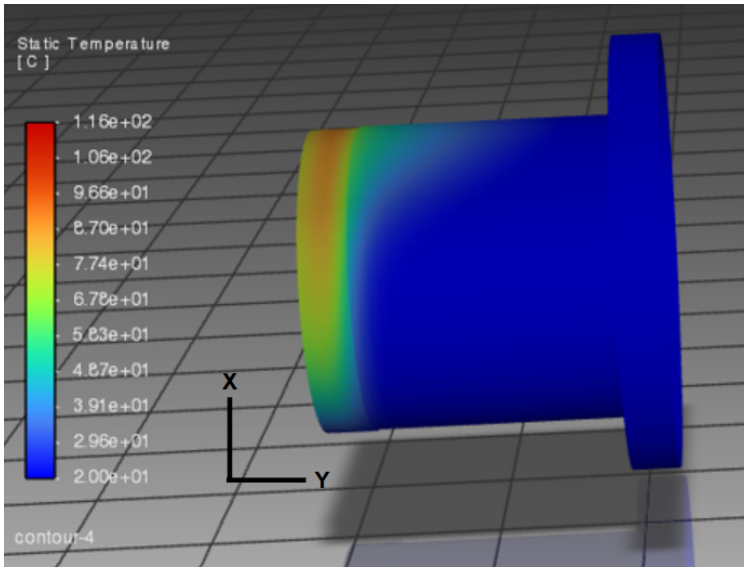

Figure 3.10: Temperature distribution results after running a simulation in ANSYS Fluent. The plume of hot water rises up (+ x direction), displaying effects of natural convection. Gravity is being applied in the negative x direction (9.81 m/s^2). The compartment shown is the target water chamber, with the first 2.5 m being heated by the beam. This data was collected using 50 time steps (0.1 s each).

Figure 3.11 displays the pressure across the system. The target chamber base is a fully enclosed chamber, so it makes sense that the pressure rapidly builds here as it is heated. At the velocity inlets, the pressure is higher due to coolant being injected. Coolant exits the pressure outlets at a lower pressure. Displaying the pressure distribution acted as a checkpoint to ensure the inlets and outlets were correctly set up.

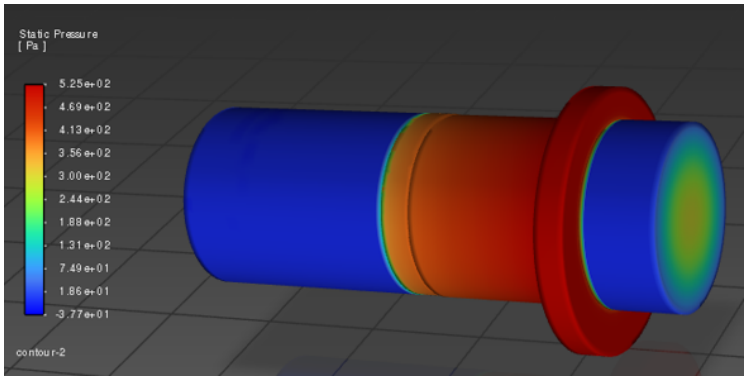

Figure 3.11: Static pressure across the model during an ANSYS Fluent simulation run. Higher pressure is displayed at the inlets of the coolant sources, as well as within the liquid target chamber.

When a simulation is initiated, many hundreds of iterations are run where the solver

attempts to solve the selected equations for the system. After each iteration, Fluent determines how far off the modelled solution matches the actual physics of the system. This difference, the error, is called the residual. Each iteration tries to improve the results from the last, minimizing the residuals until they plateau. This is how the solver reduces error in the simulation results. The scaled residual plot for the energy displays the oscillatory peak behaviour. This was expected due to the interconnectedness of the flow and thermodynamics of the system. The rise is due to large initial changes due to heating, then as the model stabilizes, the peak falls. This process is repeated each time heat is added to the system, causing oscillatory behaviour.

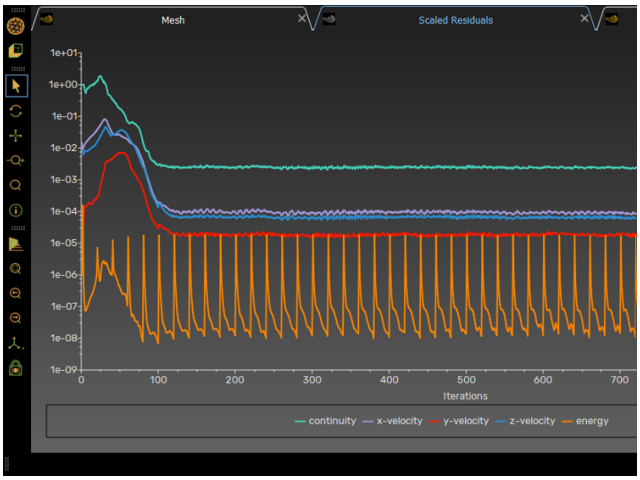

Figure 3.12: Scaled Residual curve of velocity in x, y, and z directions, energy, and continuity. Taken from ANSYS Fluent run.

The simulation results using a k-ω turbulence model showed better agreement with the measured temperature data than the ANSYS mechanical runs. Natural convection occurs across the system, with warmer water rising. Laminar Flow and k-ϵ turbulence models were also attempted; however, they did not provide the desired physical effect. The k-ϵ model mixed the fluid too aggressively, making heat-driven natural convection difficult to see. The Laminar flow model displayed the natural convection effect, but little heat remained in the center of the target. Since this type of flow modelling involves little mixing, with heat rising in smooth, parallel layers, it does not capture the physics observed in actual cyclotron targets. The k-ω model displayed middle ground behaviour between these two models, providing the best agreement to the measured thermal data.

The ANSYS Fluent simulation results had much stronger agreement with the measured temperature data than the Mechanical runs. The temperature at each FBG indicates that natural convection was occurring throughout the system. However, for higher beam currents, the model deviates more from the measured values. These deviations could be due to improper cooling across the system, or from more complicated flow in the target that is not currently being accurately modelled.

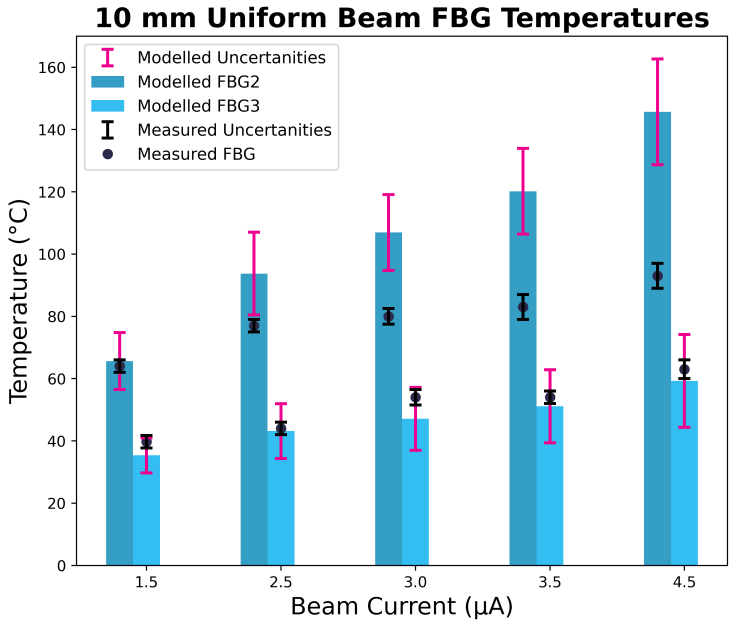

Figure 3.13: Measured and modelled temperature values at each FBG position [1]. Uncertainties for the measured and modelled FBG values were found using the same approach illustrated in Calculations 3-9.

Table 3.13: Final transient k-ω model results.

Beam Current (μA)	**Max (°C)**	**FBG 2 (°C)**	**FBG 3 (°C)**
1.5	134	65.648	35.348
2.5	211	93.730	43.148
3.0	247	106.936	47.082
3.5	283	120.157	51.110
4.5	354	145.694	59.243

3.6 Redesigning the Target Cooling Chamber

Time was taken to create a SolidWorks part file of a modified Target Cooling Chamber. Redesigning the target cooling chamber could increase the rate of cooling in the system. The original design was modified by adding aluminum fins to the chamber, potentially allowing more avenues for heat to escape.

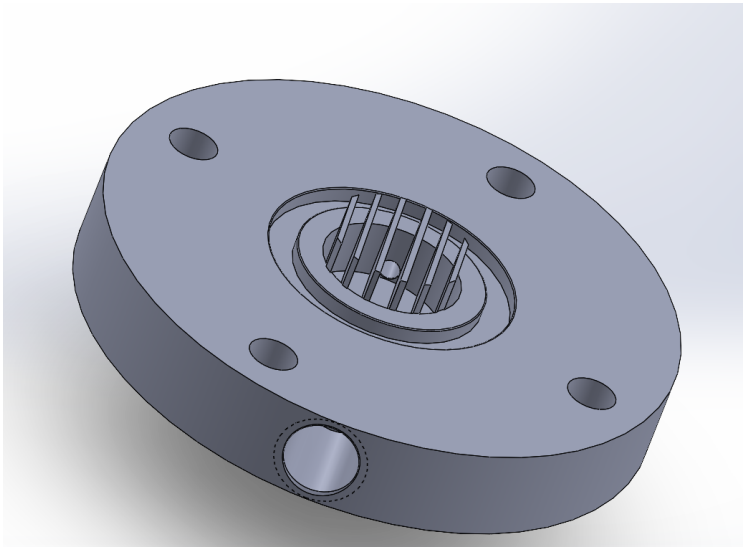

Figure 3.15: SolidWorks part file displaying the modified target cooling chamber with fins.

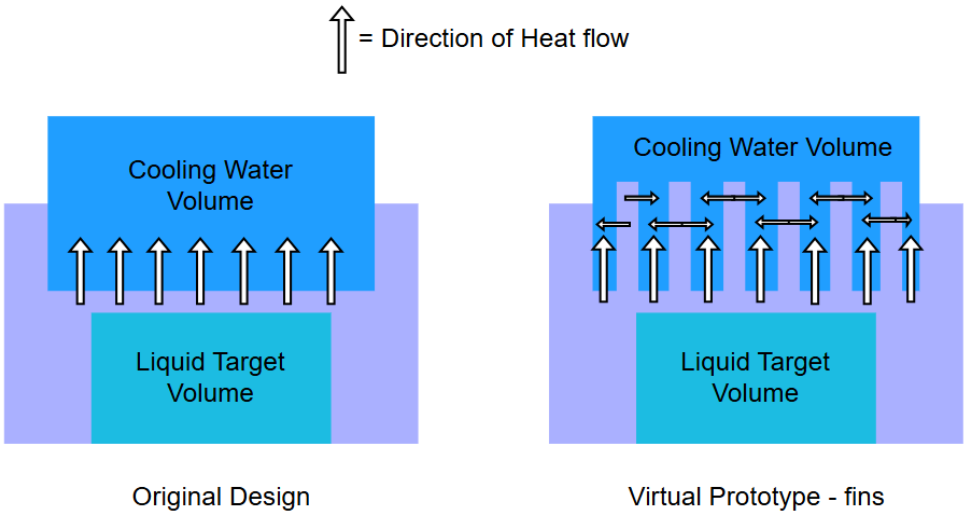

Figure 3.14: The original target cooling chamber versus the modified target cooling chamber. Adding fins increases the surface area and creates more avenues for heat to escape (shown by white arrows in Figure 3.14), potentially allowing for increased cooling across the system.

The significance of this virtual prototype is that increasing cooling across the system could result in increased yields, allowing more patients globally to have access to life-saving imaging and treatment techniques that utilize radioisotopes.

Chapter 4

Conclusion

SolidWorks was used to create a CAD model of the liquid target from draft drawings provided by TRIUMF. This software was also used to create a virtual prototype to be used in simulations in the future. SRIM/TRIM provided beam data displaying the expected behaviour of a 13 MeV proton beam. The Bragg peak occurred within the first 2.5 mm of the target water region, and the beam profile was strongly centered on axis, dispersing radially outward.

ANSYS Mechanical does not provide the proper framework to model the thermal behaviour of a liquid cyclotron target. This is a result of the software lacking the capacity to model fluid flow, meaning natural convective and boiling effects are absent from the simulation. This applies for both a uniform 10 mm beam, as well as an approximated Gaussian 10 mm beam. ANSYS Fluent was able to model the thermal behaviour of the liquid target using a k-ω turbulence model. These results displayed stronger agreement with the measured temperature data than the ANSYS mechanical simulations. Specifically, the Boussinesq approximation applied to the target water region resulted in buoyancy-driven flow throughout the system. As the beam current increased, the agreement between the modelled and measured values at FBG2 decreased: the model began to overpredict temperatures at FBG2. This indicates that there are still limiting factors present in the model, such as inadequate representation of cooling or inaccurate modelling of water's viscous behaviour near its boiling point

This work supports the ongoing effort to optimize medical radioisotope production by advancing the development of a reliable computational thermal model of a liquid cyclotron target. The ANSYS Fluent model established here still has further improvements needed before it can be fully trusted. Specifically, narrowing the gap between modelled and measured data at higher beam currents is the key remaining step. Once the model successfully reproduces observed thermal measurements, such a model would enable virtual prototyping. Through this, scientists and engineers can test a wide range of target designs in a fraction of the time required to physically construct and irradiate them. A trusted thermal model that helps minimize boiling within the target could improve radioisotope yields, helping to expand patient access to life-saving diagnostic imaging and treatment techniques worldwide.

Chapter 5

Future Work

To monitor how the heat behaves within the target's canister, the temperature at the location of FBG1 should be included in future thermal modelling using ANSYS Fluent simulations. Although the temperatures at FBG2 and FBG3 show the same trend as the measured temperature values, displaying natural convection, they deviate more strongly as the beam current is increased. Further investigation into the cooling and mixing of fluid within the model is required to minimize this deviation.

A further potential improvement to the model is a more accurate representation of the proton beam profile. The current model assumes that the beam displays Gaussian behaviour, but in reality, the beam deviates from true Gaussian form [22]. Specifically, more particles are present at larger radii than a Gaussian beam expects; these are known as tails [22]. This deviation affects the lateral distribution of energy deposited within the target, and consequently, the heat generation profile applied during the thermal simulation.

Further investigation into the thermal contribution of the Helium cooling is needed to determine its overall efficacy in managing the heat load generated across the target. If the Helium coolant is found to provide a negligible reduction in peak temperatures, a transition to a water-cooled (at downstream end of target only) design using fins could be explored. Water has a higher heat capacity and thermal conductivity than Helium, which would facilitate more efficient heat dissipation. Additionally, the ambient air-cooling in the radial direction should be taken into account in future simulations. This ambient air may be hotter than room temperature, since it is a confined space exposed to the heat generated from the cyclotron resistive magnet.

Once a reliable computational thermal model is produced, the next step would be to begin virtual prototyping of the model. This is, to test many possible design modifications via simulations, instead of taking time to physically construct and irradiate new liquid cyclotron targets. During this research project, a possible design modification involving fins was looked into to improve overall cooling. Simulations could be run with this new component replacing the previous target cooling chamber. Additional modifications to improve cooling across the system include replacing the cooling chamber material with a higher-conductivity metal, such as copper or silver, and adjusting the coolant flow rate. If the simulated FBG temperatures decrease, this indicates increased cooling. This new compo-

nent could also be physically manufactured and put into a liquid cyclotron target to test the model's predictions. This would allow us to directly test if a greater yield results, or if something else is missing from the model.

Bibliography

[1] Dehnel G. *Thermal measurements of medical isotope targets* [Master's thesis]. Kelowna (BC): University of British Columbia Okanagan Campus; 2025.

[2] Wang Y, et al. Production Review of Accelerator-Based Medical Isotopes. Molecules. 2022;27(16):5294. doi: 10.3390/molecules27165294. Available from: `www.mdpi.com/1420-3049/27/16/5294`

[3] Bakaic M, et al. Fiber-Optic Bragg Gratings for Temperature and Pressure Measurements in Isotope Production Targets for Nuclear Medicine. *Applied Sciences*. 2020 Jul;10(13):4610. doi: 10.3390/app10134610. Available from: `www.mdpi.com/2076-3417/10/13/4610`

[4] Canadian Cancer Society / Société canadienne du cancer. "Cancer Statistics at a Glance." Canadian Cancer Society, cancer.ca/en/research/cancer-statistics/cancer-statistics-at-a-glance.

[5] "Radiation Therapy." BC Cancer Foundation, 28 Nov. 2025, bccancerfoundation.com/why-give/research/radiation-therapy/.

[6] Canadian Cancer Society / Société canadienne du cancer. "Positron Emission Tomography (PET) Scan." Canadian Cancer Society, cancer.ca/en/treatments/tests-and-procedures/positron-emission-tomography-pet-scan.

[7] "Single Photon Emission Computed Tomography (SPECT)." Single Photon Emission Computed Tomography (SPECT) — HealthLink BC, www.healthlinkbc.ca/healthwise/single-photon-emission-computed-tomography-spect.

[8] "Brachytherapy." Mayo Clinic, Mayo Foundation for Medical Education and Research, 19 June 2024, www.mayoclinic.org/tests-procedures/brachytherapy/about/pac-20385159.

[9] Rydén, Jenny. "Women Who Changed Science - Marie Curie." NobelPrize.Org, 20 Aug. 2025, www.nobelprize.org/stories/women-who-changed-science/marie-curie/.

[10] "Radioisotopes in Medicine." World Nuclear Association, world-nuclear.org/information-library/non-power-nuclear-applications/radioisotopes-research/radioisotopes-in-medicine.

[11] Peeples, Johanna L., et al. "Thermal performance of batch boiling water targets for 18F production." Applied Radiation and Isotopes, vol. 69, no. 10, Oct. 2011, pp. 1349–1354,

doi: doi.org/10.1016/j.apradiso.2011.06.015 Available from: www.sciencedirect.com/science/article/abs/pii/S0969804311003563/

[12] Bakaic M, et al. Fiber-Optic Bragg Gratings for Temperature and Pressure Measurements in Isotope Production Targets for Nuclear Medicine. *Applied Sciences*. 2020 Jul;10(13):4610. doi: 10.3390/app10134610. Available from: www.mdpi.com/2076-3417/10/13/4610

[13] CERN. "Medical-Isotope Cyclotron Designs Go Full Circle." CERN Courier, 22 Oct. 2021, cerncourier.com/a/medical-isotope-cyclotron-designs-go-full-circle/.

[14] "Pet Cyclotron and Radiopharmacy Facility." PET Cyclotron and Radiopharmacy Facility, www.bccancer.bc.ca/our-services/services/molecular-imaging-therapy/pet-cyclotron-and-radiopharmacy-facility.

[15] Solidworks2025 [Computer Software], Dassault Systèmes S.A.. www.solidworks.com

[16] Ziegler, James F. (2008). SRIM - The Stopping and Range of Ions in Matter [Computer Software]. www.srim.org

[17] Ansys, Release 2025R2, Synopsys. www.ansys.com

[18] Al-Yahia, Omar S., and Daeseong Jo. "Onset of nucleate boiling for subcooled flow through a one-side heated narrow rectangular channel." Annals of Nuclear Energy, vol. 109, Nov. 2017, pp. 30–40, doi: doi.org/10.1016/j.anucene.2017.05.014.

[19] "Havar (Alloy)." Wikipedia, Wikimedia Foundation, 10 Dec. 2025, en.wikipedia.org/wiki/Havar_(alloy).

[20] Pope, S. B. (2000). Turbulent Flows. Cambridge University Press.

[21] Gray, Donald D. and Giorgini, Aldo. "The validity of the Boussinesq approximation for liquids and gases." International Journal of Heat and Mass Transfer, 1976, doi: doi.org/10.1016/0017-9310(76)90168-X. Available from www.sciencedirect.com/science/article/abs/pii/001793107690168X?via%3Dihub

[22] R.E. Laxdal, A. Altman, T. Kuo, and T. Kadantsev, "Beam Measurements on a Small Commercial Cyclotron." *Proceedings of the European Particle Accelerator Conference (EPAC94)*, London, 1994, pp. 545–547.

[23] K.R. Buckley. "D-Pace Faraday Cup design review" March 15, 2007

Chapter 6

Appendix

6.0.1 Python Code

```
[2]: import numpy as np
     import matplotlib.pyplot as plt
     import pandas as pd
```

```
[139]: df = pd.read_csv("EXYZ_Oct17.txt",delim_whitespace=True, skiprows=range(0, 14),
                        names=["Ion Number", "Energy_keV", "Depth_A", "Y_A",
        ↪"Z_A","Electronic_Stop", "Energy_Lost"])

       df = df[["Depth_A", "Energy_keV"]] #these are the only columns I care about
       #I should note the depth is in angstroms (10^-10 m).
       #I will convert the thickness because the depth is in angstoms i think
       al_thickness = 25*10000 #um to angstroms
       havar_thickness = 39*10000 #um to angstroms
       water_thickness = 17.55*1*10**(7) #mm to angstroms

       #i was getting an error because these columns are strings, so i need to make
        ↪them numeric values
       df["Depth_A"] = pd.to_numeric(df["Depth_A"], errors="coerce")
       df["Energy_keV"] = pd.to_numeric(df["Energy_keV"], errors="coerce")
       #this drops any remaining header text or things that couldn't convert to numeric
       df = df.dropna(subset=["Depth_A", "Energy_keV"])

       al_energy = df.loc[(df['Depth_A'] - al_thickness).abs().idxmin(), 'Energy_keV']
       havar_energy = df.loc[(df['Depth_A']- (al_thickness + havar_thickness)).abs().
        ↪idxmin(), 'Energy_keV']
       water_energy = df.loc[(df['Depth_A'] - (al_thickness +havar_thickness +
        ↪water_thickness)).abs().idxmin(), 'Energy_keV']

       print(f"Energy at end of Al layer: {al_energy:.2f} keV")
       print(f"Energy at end of Havar layer: {havar_energy:.2f} keV")
       print(f"Energy at end of Water layer: {water_energy:.2f} keV")
       #I am subtracting the deposited foil energies because I want the energy
        ↪deposited in each layer to be specific
       #for that layer
       al_deposited = 13*10**3- al_energy
       havar_deposited  = al_energy- havar_energy #taking the difference of the
        ↪energies at the boundaries
```

```
       water_deposited  = havar_energy - water_energy
       print(f"Energy deposited in Al layer: {al_deposited:.2f} keV")
       print(f"Energy deposited in Havar layer: {havar_deposited:.2f} keV")
       print(f"Energy deposited in Water layer: {water_deposited:.2f} keV")
```

Figure 6.1: Python code used to determine the fraction of beam energy deposited to each material in the liquid target. 10 mm uniform 13 MeV proton beam.

[43]:
```python
#this is the total energy based on uniform energy deposition
total_energy = {"Al": 192.0, "Havar": 841.0, "Water": 11966.01}

radii = [0, 2, 3.5, 4.5, 5]
sigma = 1.5  #mm


def gaussian_ring_energy(E_total, r_in, r_out, sigma):
    #f is the fraction of energy in each ring
    f = np.exp(-r_in**2/(2*sigma**2)) - np.exp(-r_out**2/(2*sigma**2))
    return E_total * f

#compute the power deposited in each ring based on a provided current
current = 4.5
for layer, E in total_energy.items():
    ring_energies = []
    ring_powers = []
```

```python
    for i in range(4):
        E_ring = gaussian_ring_energy(E, radii[i], radii[i+1], sigma)
        P_ring = E_ring / 1000 *current #dividing by 1000 gets it in MeV from␣
↪keV
        P_ring = round(P_ring, 4)
        ring_energies.append(E_ring)
        ring_powers.append(P_ring)
    print(f"{layer} Power deposited per ring (keV) at {current} muA (inner to␣
↪ring3): {ring_powers} W")
```

```
Al Power deposited per ring (keV) at 4.5 muA (inner to ring3): [0.5088, 0.2984,
0.0472, 0.0063] W
Havar Power deposited per ring (keV) at 4.5 muA (inner to ring3): [2.2286,
1.3071, 0.2067, 0.0274] W
Water Power deposited per ring (keV) at 4.5 muA (inner to ring3): [31.7099,
18.5979, 2.9411, 0.39] W
```

Figure 6.2: Python code used to determine the fraction of beam energy and power deposited to each ring of material in the liquid target. 10 mm rough Gaussian 13 MeV proton beam.

[12]:
```python
import numpy as np

#these are the boundaries of the rings
radii = [0, 2, 3.5, 4.5, 5]
sigma = 1.5  #in mm

#these are the q0 values, I might have to try to calculate peak q0 values␣
 ↪instead actually
q0_values = {
    "Water": 27.424052e7,
    "Aluminum":  4.400305e8,
    "Havar": 1.18999036e9
}

def gaussian_ring_qavg(q0, r_in, r_out, sigma):
  #finds how much power is deposited into each ring
    numerator = 2 * q0 * sigma**2 * (
        np.exp(-r_in**2 / (2 * sigma**2)) -
        np.exp(-r_out**2 / (2 * sigma**2))
    )
    denominator = r_out**2 - r_in**2
    return numerator / denominator

#doing this for each ring
for material, q0 in q0_values.items():
    ring_q = []
    for i in range(4):
        q_ring = gaussian_ring_qavg(
            q0,
            radii[i],
            radii[i+1],
            sigma
        )
        ring_q.append(q_ring)

    print(f"{material} volumetric heat generation per ring (W/m^3):")
    print([f"{q:.3e}" for q in ring_q])
    print()
```

```
Water volumetric heat generation per ring (W/m^3):
['1.817e+08', '5.166e+07', '8.426e+06', '1.882e+06']

Aluminum volumetric heat generation per ring (W/m^3):
['2.915e+08', '8.290e+07', '1.352e+07', '3.019e+06']

Havar volumetric heat generation per ring (W/m^3):
['7.884e+08', '2.242e+08', '3.656e+07', '8.166e+06']
```

Figure 6.3: Python code used to determine the heat generation values (W/m^2) related to each ring segment of material in the liquid target. 10 mm rough Gaussian 13 MeV proton beam.

6.0.2 ANSYS Mechanical Data

Table 6.1: ANSYS Mechanical simulation development results showing progression of thermal model refinements.

h	**I (μA)**	**Max (°C)**	**Min (°C)**	**FBG 3 (°C)**	**FBG 2 (°C)**	**Note**
Uniform beam — power volume corrections						
875	1.5	125.49	20.00	69.00	64.000	a
875	1.5	208.37	7.01	57.88	39.310	b
875	1.5	198.99	16.55	44.42	31.480	b
2500	1.5	238.68	15.47	50.45	34.170	c
875	1.5	289.86	14.68	56.62	37.240	c
Gaussian beam — W/m^3 corrections						
875	1.5	97.92	19.40	26.85	22.270	d
875	1.5	448.57	15.77	56.30	31.140	e
2500	1.5	395.30	16.74	51.07	29.330	e
750	1.5	459.07	15.60	57.33	31.520	e
400	1.5	506.06	14.86	62.04	33.300	e
Higher beam currents						
875	2.5	468.94	10.93	80.84	48.580	f
875	2.5	733.27	12.83	80.21	38.340	e
600	2.5	777.97	12.11	84.63	39.990	e
875	3.0	558.49	9.07	92.95	54.260	f
875	3.5	648.04	7.21	105.07	59.940	f
4.5μA — water cooling corrections						
700	4.5	969.87	2.90	142.24	76.580	g
1000	4.5	931.92	2.93	134.84	72.680	g
875	4.5	948.92	16.15	136.32	73.993	h
875	4.5	946.76	16.17	135.92	73.782	i

Notes:
a — Pre-Gaussian beam profile.
b — 10 mm beam, beam misalignment present.
c — 10 mm beam, corrected power volumes.
d — Rough Gaussian, incorrect W/m^3 values.
e — Rough Gaussian, peak q_0 W/m^3 values.
f — 10 mm beam, standard settings.
g — Uniform beam, water cooling issue present.
h — Uniform beam, water cooling corrected.
i — Uniform beam, Havar W/m^3 corrected.

6.0.3 ANSYS Mechanical Rough Gaussian Runs

Table 6.2: Power deposited per annular ring region in each material at 2.5 μA (inner to outer).

Ring	**Al (W)**	**Havar (W)**	**Water (W)**
Inner	0.2827	1.2381	17.6166
Ring 1	0.1658	0.7262	10.3322
Ring 2	0.0262	0.1148	1.6339
Ring 3	0.0035	0.0152	0.2167
Total	0.4782	2.0943	29.7994

Table 6.3: Power deposited per annular ring region in each material at 3.0 μA (inner to outer).

Ring	**Al (W)**	**Havar (W)**	**Water (W)**
Inner	0.3392	1.4858	21.1399
Ring 1	0.1989	0.8714	12.3986
Ring 2	0.0315	0.1378	1.9607
Ring 3	0.0042	0.0183	0.2600
Total	0.5738	2.5133	35.7592

Table 6.4: Power deposited per annular ring region in each material at 3.5 μA (inner to outer).

Ring	**Al (W)**	**Havar (W)**	**Water (W)**
Inner	0.3957	1.7334	24.6632
Ring 1	0.2321	1.0166	14.4650
Ring 2	0.0367	0.1608	2.2875
Ring 3	0.0049	0.0213	0.3033
Total	0.6694	2.9321	41.7190

Table 6.5: Power deposited per annular ring region in each material at 4.5 μA (inner to outer).

Ring	**Al (W)**	**Havar (W)**	**Water (W)**
Inner	0.5088	2.2286	31.7099
Ring 1	0.2984	1.3071	18.5979
Ring 2	0.0472	0.2067	2.9411
Ring 3	0.0063	0.0274	0.3900
Total	0.8607	3.7698	53.8389

Table 6.6: Volumetric heat generation (W/m^3) per annular ring region for each material and beam current (μA).

Current (μA)	**Material**	**Inner**	**Ring 1**	**Ring 2**	**Ring 3**
1.5	Water	6.056×10^7	1.722×10^7	2.809×10^6	6.273×10^5
	Al	9.717×10^7	2.763×10^7	4.506×10^6	1.006×10^6
	Havar	2.628×10^8	7.473×10^7	1.219×10^7	2.722×10^6
2.5	Water	1.009×10^8	2.870×10^7	4.681×10^6	1.045×10^6
	Al	1.620×10^8	4.605×10^7	7.511×10^6	1.677×10^6
	Havar	4.380×10^8	1.245×10^8	2.031×10^7	4.536×10^6
3.0	Water	1.211×10^8	3.444×10^7	5.617×10^6	1.255×10^6
	Al	1.943×10^8	5.527×10^7	9.013×10^6	2.013×10^6
	Havar	5.256×10^8	1.495×10^8	2.437×10^7	5.444×10^6
3.5	Water	1.413×10^8	4.018×10^7	6.553×10^6	1.464×10^6
	Al	2.267×10^8	6.448×10^7	1.051×10^7	2.348×10^6
	Havar	6.132×10^8	1.744×10^8	2.844×10^7	6.351×10^6
4.5	Water	1.817×10^8	5.166×10^7	8.426×10^6	1.882×10^6
	Al	2.915×10^8	8.290×10^7	1.352×10^7	3.019×10^6
	Havar	7.884×10^8	2.242×10^8	3.656×10^7	8.166×10^6

Units: W/m^3

6.0.4 Positional Sensitivity Analysis Data

Table 6.7: Positional sensitivity results at 1.5 μA, $h = 875\,W/m^2K$.

Configuration	**Position**	**Max (°C)**	**Min (°C)**	**FBG 3 (°C)**	**FBG 2 (°C)**
Original	0	289.81	14.514	56.550	37.166
Displaced	+0.5 mm	301.24	17.791	59.563	38.529
Displaced	+1.0 mm	301.93	17.702	59.794	38.551
Displaced	-0.5 mm	303.02	8.706	58.687	37.440
Displaced	-1.0 mm	290.87	14.872	56.957	36.687
Rotated	90°	437.36	17.220	63.619	40.785

Table 6.8: Positional sensitivity results at 2.5 μA, $h = 875\,\mathrm{W/m^2K}$.

Configuration	**Position**	**Max (°C)**	**Min (°C)**	**FBG 3 (°C)**	**FBG 2 (°C)**
Original	0	517.58	14.876	85.005	50.070
Displaced	+0.5 mm	696.27	3.510	93.107	52.545
Displaced	+1.0 mm	560.29	17.985	84.852	50.831
Displaced	-0.5 mm	501.78	3.316	84.726	49.252
Displaced	-1.0 mm	471.46	6.376	82.047	48.015
Rotated	90°	717.62	10.805	92.456	54.841

Table 6.9: Positional sensitivity results at 3.0 μA, $h = 875\,\mathrm{W/m^2K}$.

Configuration	**Position**	**Max (°C)**	**Min (°C)**	**FBG 3 (°C)**	**FBG 2 (°C)**
Original	0	638.07	17.438	97.338	55.897
Displaced	+0.5 mm	663.11	11.840	99.147	56.478
Displaced	+1.0 mm	662.71	17.601	97.693	56.690
Displaced	-0.5 mm	580.59	10.102	96.660	54.739
Displaced	-1.0 mm	560.52	17.752	93.578	53.275

Table 6.10: Positional sensitivity results at 3.5 μA, $h = 875\,\mathrm{W/m^2K}$.

Configuration	**Position**	**Max (°C)**	**Min (°C)**	**FBG 3 (°C)**	**FBG 2 (°C)**
Original	0	740.56	16.987	110.190	61.866
Displaced	+0.5 mm	770.13	10.484	112.320	62.549
Displaced	+1.0 mm	769.64	17.202	110.620	62.797
Displaced	-0.5 mm	673.87	8.457	109.420	60.519
Displaced	-1.0 mm	650.42	17.378	105.820	58.811

Table 6.11: Positional sensitivity results at 4.5 μA, $h = 875\,\mathrm{W/m^2K}$.

Configuration	**Position**	**Max (°C)**	**Min (°C)**	**FBG 3 (°C)**	**FBG 2 (°C)**
Original	0	948.38	16.118	136.290	73.986
Displaced	+0.5 mm	987.30	7.705	139.060	74.869
Displaced	+1.0 mm	986.97	16.395	136.880	75.185
Displaced	-0.5 mm	863.00	5.125	135.340	72.270
Displaced	-1.0 mm	833.99	16.621	130.730	70.081

6.0.5 Helium Heat Transfer Coefficient (h) Analysis Data

Table 6.12: Effect of varying Helium heat transfer coefficient h (W/m^2K) on thermal model results.

h **(W/m^2K)**	**Beam Current (μA)**	**Max (°C)**	**Min (°C)**	**FBG 3 (°C)**	**FBG 2 (°C)**
750	1.5	334.79	18.641	59.805	38.586
800	1.5	332.00	18.664	59.377	38.360
875	1.5	329.44	18.696	58.797	38.052
975	1.5	325.96	18.733	58.119	37.692
750	2.5	544.11	17.760	86.192	50.861
875	2.5	535.21	17.854	84.503	49.962
975	2.5	529.40	17.917	83.366	49.356
1050	2.5	525.56	17.959	82.612	48.953

6.0.6 ANSYS Fluent Data

Table 6.13: Transient thermal model development log showing iterative refinements. Created using ANSYS Fluent runs.

Solver Setup	I (μA)	Max (°C)	FBG 2 (°C)	FBG 3 (°C)	Note
Steady-state convergence tests					
100 iterations	1.5	32.0	26.849	27.184	j
500 iterations	1.5	32.0	26.850	26.850	a,j
100 iterations	1.5	57.0	20.000	20.000	b,j
Transient — varying coolant flow rate					
50 steps (0.1 s)	1.5	116.0	36.801	20.036	c,j
50 steps (0.2 s)	1.5	168.1	65.591	20.669	c,j
50 steps (0.3 s)	1.5	200.1	86.540	24.806	c,j
50 steps (0.2 s)	1.5	168.1	65.591	20.669	d,j
50 steps (0.2 s)	1.5	182.1	65.255	22.497	e,j
50 steps (0.2 s)	1.5	182.1	65.255	22.497	f,j
50 steps (0.2 s)	1.5	182.1	65.258	22.497	g,j
100 steps (0.5 s)	1.5	294.0	169.000	83.000	f,j
Transient — varying beam current, flow = 0.1					
50 steps (0.2 s)	1.5	182.0	65.250	22.497	j
50 steps (0.2 s)	2.5	278.0	61.340	25.668	j
50 steps (0.2 s)	2.5	278.0	97.013	25.668	h,j
50 steps (0.2 s)	2.5	278.0	96.997	25.663	i,j
50 steps (0.2 s)	3.0	324.0	112.289	27.527	j
50 steps (0.2 s)	3.5	369.0	127.448	29.560	j
50 steps (0.2 s)	4.5	456.0	157.520	33.926	j
Turbulence model investigation					
50 steps (0.2 s)	1.5	189.0	67.660	29.664	j
50 steps (0.2 s)	1.5	56.4	35.186	35.187	k
100 steps (0.2 s)	1.5	61.3	42.720	42.721	k
100 steps (0.2 s)	1.5	59.8	42.468	42.469	l
100 steps (0.2 s)	1.5	69.5	43.811	43.815	m
100 steps (0.2 s)	1.5	134.0	65.648	35.348	n
100 steps (0.2 s)	2.5	223.0	111.064	53.808	n
75 steps (0.2 s)	2.5	211.0	93.730	43.148	n
75 steps (0.2 s)	3.0	247.0	106.936	47.082	n
75 steps (0.2 s)	3.5	283.0	120.157	51.110	n
75 steps (0.2 s)	4.5	354.0	145.694	59.243	n

Notes:
a — Solution converged.
b — Steady state confirmed.
c — Coolant flow rate = 0.0001 m/s.
d — Coolant flow rate = 0.01 m/s.
e — Coolant flow rate = 0.01 m/s, coupled mesh interfaces.
f — Coolant flow rate = 0.1 m/s.
g — Coolant flow rate = 0.5 m/s.
h — Coupled mesh interfaces applied.
i — Matched mesh interfaces applied.
j — Laminar flow model.
k — k-ε turbulence model.
l — k-ε model with adjusted settings.
m — k-ε model, turbulent Prandtl number $\mathrm{Pr}_t = 1.5$.
n — k-ω turbulence model.